

# Augmented Empirical Models of Plasmaspheric Density and Electric Field Using IMAGE and CLUSTER Data

Bodo W. Reinisch · Mark B. Moldwin · Richard E. Denton · Dennis L. Gallagher · Hiroshi Matsui · Viviane Pierrard · Jiannan Tu

Received: 7 July 2008 / Accepted: 2 December 2008 / Published online: 3 February 2009  
© Springer Science+Business Media B.V. 2009

**Abstract** Empirical models for the plasma densities in the inner magnetosphere, including plasmasphere and polar magnetosphere, have been in the past derived from in situ measurements. Such empirical models, however, are still in their initial phase compared to magnetospheric magnetic field models. Recent studies using data from CRRES, POLAR, and IMAGE have significantly improved empirical models for inner-magnetospheric plasma and mass densities. Comprehensive electric field models in the magnetosphere have been developed using radar and in situ observations at low altitude orbits. To use these models at high altitudes one needs to rely strongly on the assumption of equipotential magnetic field lines.

---

B.W. Reinisch (✉) · J. Tu  
Department of Environmental, Earth and Atmospheric Sciences, University of Massachusetts-Lowell (UML), 600 Suffolk Street, Lowell, MA 01854, USA  
e-mail: [bodo\\_reinisch@uml.edu](mailto:bodo_reinisch@uml.edu)

J. Tu  
e-mail: [jiannan\\_tu@uml.edu](mailto:jiannan_tu@uml.edu)

M.B. Moldwin  
Institute of Geophysics and Planetary Physics (IGPP), University of California, Los Angeles, CA, USA  
e-mail: [mmoldwin@igpp.ucla.edu](mailto:mmoldwin@igpp.ucla.edu)

R.E. Denton  
Physics and Astronomy Department, Dartmouth College, Hanover, NH, USA  
e-mail: [richard.e.denton@dartmouth.edu](mailto:richard.e.denton@dartmouth.edu)

D.L. Gallagher  
Marshall Space Flight Center (MSFC), NASA, Huntsville, AL, USA  
e-mail: [dennis.l.gallagher@nasa.gov](mailto:dennis.l.gallagher@nasa.gov)

H. Matsui  
Space Science Center, University of New Hampshire (UNH), Durham, NH, USA  
e-mail: [hiroshi.matsui@unh.edu](mailto:hiroshi.matsui@unh.edu)

V. Pierrard  
Belgian Institute for Space Aeronomy (BIRA-IASB), Brussels, Belgium  
e-mail: [viviane.pierrard@oma.be](mailto:viviane.pierrard@oma.be)

Direct measurements of the electric field by the CLUSTER mission have been used to derive an equatorial electric field model in which reliance on the equipotential assumption is less. In this paper we review the recent progress in developing empirical models of plasma densities and electric fields in the inner magnetosphere with emphasis on the achievements from the IMAGE and CLUSTER missions. Recent results from other satellites are also discussed when they are relevant.

**Keywords** Inner magnetosphere · Plasmasphere · Empirical models · Plasma density · Electric field · CLUSTER · IMAGE

## 1 Introduction

Empirical models of plasma density and fields (electric and magnetic fields) play important roles in space plasma studies and space weather prediction. They provide convenient ways to represent the plasma environment around the Earth. Empirical models are important for developing physics-based numeric models as well, since they provide baseline predictions against which to measure their performance (Siscoe et al. 2004) and against which plasma density variations can be evaluated, particularly during magnetic storms (e.g., Reinisch et al. 2004; Tu et al. 2007; Osherovich et al. 2007).

Empirical models of thermal plasma densities in the inner magnetosphere have been developed over many decades. The first efforts were based on the pioneering work by Storey (1953) using ground whistler observations. Using these remote observations, we learned about the existence of the plasmopause and its responses to changing geomagnetic conditions (Pope 1961; Smith 1961; Carpenter 1963; Carpenter and Lemaire 1997; Lemaire and Gringauz 1998; Carpenter 2004). Subsequently, empirical models of the plasmopause position have been derived from in situ measurements such as by the IMP-2, ISEE-1, DE-1, and CRRES satellites (e.g., Binsack 1967; Horwitz et al. 1990; Carpenter and Anderson 1992; Moldwin et al. 2002; O'Brien and Moldwin 2003). Plasmaspheric density models have also been obtained from in situ observations (e.g., Carpenter and Anderson 1992; Gallagher et al. 1998, 2000; Sheeley et al. 2001). Similarly, there have been efforts to develop empirical plasma density models in the magnetospheric polar cap. Based on data from the above mentioned and other satellites Persoon et al. (1983) and Gallagher et al. (2000) developed polar cap density models in which density is shown to vary statistically as a power law with radial distance. The studies of Johnson et al. (2001, 2003) revealed the effects of the solar zenith angle on the plasma density at altitudes up to  $4.5 R_E$ .

The first model of the magnetospheric electric field was the semi-empirical model of Volland (1973). A similar model was also devised by Stern (1975). Maynard and Chen (1975) then introduced  $K_p$  dependence into the Volland-Stern model. Later on more sophisticated models of the electric field were developed based on parameters describing the various geophysical, geomagnetic, solar wind and interplanetary magnetic field (IMF) effects and based on radar or satellite observations (e.g., Heppner 1977; Volland 1978; Heelis et al. 1982; Feldstein et al. 1984; Sojka et al. 1986; Heppner and Maynard 1987; Holt et al. 1987; Papitashvili et al. 1994; Matsui et al. 2004; Ruohoniemi and Greenwald 2005; Weimer 2005).

In this paper, we review advances in the development of empirical models of plasma density and electric field in the inner magnetosphere resulting from the CLUSTER and Imager for Magnetopause-to-Aurora Global Exploration (IMAGE) missions. The results from other missions will be also discussed when they are relevant. The Extreme UltraViolet (EUV)

and Radio Plasma Imager (RPI) instruments on the IMAGE satellite (Burch 2000, 2003) provided the first ever ability to remotely image plasma density structures throughout the inner magnetosphere. The four-satellite constellation of the CLUSTER mission has provided multi-point in situ measurements of plasma density, electric field, and other plasma parameters (Escoubet et al. 1997). The unique measurement techniques of these missions have greatly enhanced our ability to develop empirical models of plasma density and electric field in the plasmasphere or more generally in the inner magnetosphere. More details about the missions are available elsewhere in this issue (De Keyser et al. 2008).

The plasma and field models discussed herein are for the inner magnetosphere. For the purposes of this discussion, the inner magnetosphere extends from above the ionosphere to inside the magnetopause. At low to intermediate latitudes that includes the plasmasphere, the plasmopause, the magnetospheric trough and the plasmaspheric (erosion) plume. At higher latitudes the magnetospheric trough extends into the auroral zone and higher still there is the polar cap, which completes those regions included here as part of the inner magnetosphere.

## 2 Empirical Equatorial Density Models

The plasmasphere has been studied using low frequency plasma waves from the ground (Carpenter 1966; Park et al. 1978; Clilverd et al. 1991; Loto'aniu et al. 1999; Carpenter 2004) and using spacecraft in many different orbits (polar, geosynchronous, and near-equatorial elliptical) and with a variety of instruments (plasma wave instruments, plasma analyzers, spacecraft potential probes and most recently with imagers and radio sounding) (e.g., Gringauz 1963; Chappell et al. 1971; Décréau et al. 1982; Horwitz et al. 1986; Carpenter and Anderson 1992; Moldwin et al. 1994; Reinisch et al. 2001a; Sandel et al. 2001; Sheeley et al. 2001). Throughout the years there has been a shared interest in developing empirical models of equatorial thermal plasma distributions as a means of summarizing observed plasma behavior in the inner magnetosphere and to facilitate studies of plasma waves and energetic particle dynamics, which depend on plasmaspheric plasma distributions. The advent of global plasmaspheric imaging with EUV and RPI onboard IMAGE has energized a renewed interest in the development of empirical models both directly through their measurements and in concert with other in situ instrumentation and ground ultra low frequency (ULF) wave observations. While much can yet be accomplished with the IMAGE observations and continued CLUSTER multi-spacecraft in situ measurements, the early studies in this new era are showing the way ahead.

Larsen et al. (2007) have mapped EUV observations into the solar magnetic equatorial plane and correlated the automatically derived plasmopause  $L$ -value with solar wind conditions provided by the ACE mission. The direct correlation to the solar wind provides a new look at the state of the plasmasphere as a function of the primary driver of erosion rather than through indirect measures given by geomagnetic indices. The southward component of the IMF  $B_z$ , and a magnetic merging proxy,  $\phi$  were most highly correlated with plasmopause location ( $L_{pp}$ ). The most significant correlation was obtained for separately delayed  $B_z$  and  $\phi$  as given in the expression

$$L_{pp} = 0.0374B_{z,155} - 1.05 \times 10^{-4}\phi_{275} + 4.38, \quad (1)$$

where the numerical subscripts refer to the corresponding best fit delays in minutes. The merging proxy is defined by

$$\phi = vB \sin^2(\theta/2), \quad (2)$$

where  $v$  is the solar wind speed,  $B$  is the total IMF strength, and  $\theta$  is the solar wind clock angle. A single plasmopause location was obtained from each of the 1356 EUV images used in the correlation analysis. Each plasmopause  $L$ -shell location is the average of all plasmopause locations derived from a given EUV image. The delay times (155 min for  $B_z$  and 275 min for  $\phi$ ) well exceed average propagation time from ACE to the magnetosphere. The predictive capability of the plasmopause location is thus achieved a few hours in advance. The delay time for IMF  $B_z$  could reflect the response time of the plasmopause location to the convection after  $B_z$  changes. The delay for  $\phi$  longer than  $B_z$  is similar to the time scale of the ionospheric shielding indicating a possible relation between shielding and plasmopause motion. Larsen et al. (2007) offers that future work will differentiate the plasmopause location for varying magnetic local time (MLT) as a function of solar wind conditions.

In the course of examining the variation of electron density along magnetic field lines in the plasmasphere and in the magnetospheric trough, Reinisch et al. (2004) and Tu et al. (2006) developed empirical event models using RPI radio sounding data. In both studies, a density profile of  $L^{-4}$  in the magnetic equatorial plane reasonably describes the density distribution over the  $L$ -shell range of observations ( $1.6 < L < 7$ ) in both the plasmasphere and trough. This radial trough profile agrees with that derived by Sheeley et al. (2001) (where  $n_{eq} \propto L^{-4}$ ), which is more steep than that in Denton et al. (2004) (where  $n_{eq} \propto \bar{R}_{max}^{-3.45}$ ,  $\bar{R}_{max} = LR_E$  for a dipole field), but is less steep than that obtained by Carpenter and Anderson (1992) (where  $n_{eq} \propto L^{-4.5}$ ). In contrast, this profile is steeper than that found by Carpenter and Anderson (1992) (where  $n_{eq} \propto 10^{-0.3145L}$ ) in the plasmasphere. Tu et al. (2006) parameterized their plasmasphere and trough models using expressions similar to those used by Huang et al. (2004). Tu et al. (2006) suggested that the functional form used in their study might be of potential for developing a global plasmasphere and trough empirical model that describes both the equatorial plasma distribution and the field-aligned distribution above the topside ionosphere.

Denton et al. (2006a) also demonstrated an approach for developing an event-based empirical plasmaspheric model, except in this case using multiple data sets. They used EUV images to obtain an equatorial plasma distribution, RPI for in situ electron densities, and ground magnetometer field line resonant measurements to obtain mass densities. Functions for  $L$ -shell and MLT dependent density distributions were obtained for the inner and outer plasmasphere, for the plasmaspheric plume, for the magnetospheric trough, and for the plasmopause. A mass density model in the inner plasmasphere, outer plasmasphere, and trough was developed and used with the Denton et al. (2002b) field line dependence model. These works clearly illustrate the complexity of accurately representing thermal plasma distributions at any given time.

Berube et al. (2005) have developed the first plasmaspheric, equatorial mass density model using ground-based ULF wave measurements. RPI in situ electron densities derived from natural radio noise resonances and cut-offs were also used to develop an electron density model that when combined with the mass density model was used to infer average ion mass and composition. The electron density model was created using the results of Fung et al. (2001). Equatorial, plasmaspheric electron number densities,  $n_{eq}$ , averaged for all RPI derived values independent of geomagnetic activity were represented by the function

$$n_{eq}(L) = 10^{-0.66L+4.89}. \quad (3)$$

A similar functional form was used to fit ULF derived mass densities,  $\rho_{eq}$ . The solution for all conditions was

$$\rho_{eq}(L) = 10^{-0.67L+5.1}. \quad (4)$$

Average ion mass was derived as a function of  $L$ -shell for quiet and active conditions. Quiet time ion mass is consistent with the  $\text{He}^+/\text{H}^+$  mass ratio derived by Craven et al. (1997) based on DE-1 measurements. Significantly enhanced  $\text{O}^+$  concentrations are inferred for the outer plasmasphere during disturbed times.

### 3 Field-Aligned Density Distributions for Plasmasphere and Plasma Trough

#### 3.1 Field Line Dependence of Electron Density from in Situ Data

The average field line dependence of electron density has been studied using in situ measurements of electron density based on passive plasma wave data observed by polar orbiting spacecraft. The electron density values are determined either from the upper hybrid noise band (e.g., Benson et al. 2004) or the lower edge of the continuum radiation (e.g., LeDocq et al. 1994). The average field line dependence can be determined from an average of the electron density in latitudinal bins (Denton et al. 2002b). However, a less noisy result is found by assuming that the density values found at low and high latitude crossings of a particular  $L$  shell represent the density variation of a single flux tube. This is not exactly correct because the crossings of the same  $L$  shell are at different MLT and universal time (UT). In order to reduce the possibility of error, only orbits with smooth variations in electron density are used and the results are averaged over many crossings.

In studies based on data from the POLAR spacecraft (Denton et al. 2002a, 2002b, 2004), a power law dependence was assumed with respect to the geocentric radius,

$$n_e = n_{e0}(LR_E/R)^p, \quad (5)$$

where  $R$  is the geocentric radius,  $n_{e0}$  is the equatorial electron density and  $p$  the power law coefficient. For a dipole magnetic field, this form becomes  $n_e = n_{e0}(\cos \lambda)^{-2p}$ , where  $\lambda$  is the magnetic latitude MLAT. This equation is similar to the form used by Reinisch et al. (2004) and Huang et al. (2004) to model results from RPI active sounding

$$n_e = n_{e0}(\cos[(\pi/2)(\alpha\lambda/\lambda_{\text{inv}})])^{-\beta}, \quad (6)$$

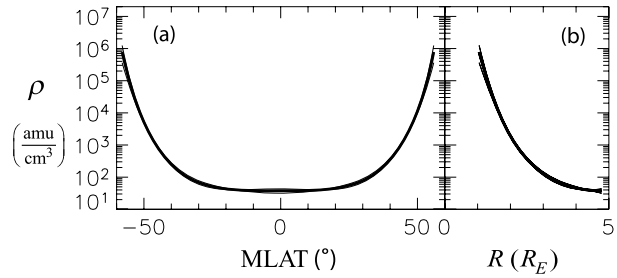
where  $\lambda_{\text{inv}}$  is the invariant latitude along the field line of the  $L$ -shell. The RPI active sounding results are effective down to an altitude of about 2000 km. Equation (5) is equivalent (for a dipole magnetic field) to (6) if  $\beta = 2p$  and  $\alpha = \lambda_{\text{inv}}/(\pi/2)$ . Denton et al. (2002a, 2004, 2006b) found that the power law coefficient  $p$  of (5) was on average 2–3 in the trough and 0–1 in the plasmasphere. In a comparison to results from RPI active sounding, Denton et al. (2002a) showed that in the plasmasphere, the upper value  $p = 1$  was more accurate.

While this method has been used predominantly for POLAR data, it can also be used with in situ electron density measurements observed by IMAGE or CLUSTER. A database of electron density measurements from passive plasma wave data observed by IMAGE has recently been created (Webb et al. 2007), partly for the purpose of doing such a study.

#### 3.2 Field Line Dependence of Mass Density Based on Spacecraft Observations of Alfvén Frequencies

Magnetospheric magnetic field lines oscillate azimuthally much like a guitar string; this oscillation has quantized (harmonic) frequencies because of the boundary condition that the field lines are “line tied” at the ionospheric boundary. Because Alfvén wave harmonics have

**Fig. 1** Mass density  $\rho$  versus magnetic latitude MLAT (*left*) and geocentric radius  $R$  (*right*) based on solutions for  $\rho$  found from Alfvén wave frequencies observed on 28 October 2002. (Adapted from Denton et al. 2009)



differing field line structure, they respond differently to mass-density depending on its field line distribution. For instance, the fundamental mode, with an antinode in the electric field perturbation (radial) and velocity perturbation (azimuthal) at the equator, is slowed down by a concentration of mass density at the magnetic equator, while the second harmonic, with a node for these quantities at the magnetic equator, is not. Thus the ratios of the harmonic frequencies can be used to infer the field line distribution of mass density, determining for instance, the  $p$  value for the power law density (5) (Denton 2006).

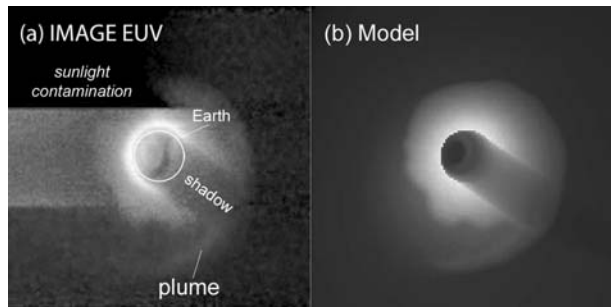
Calculations based on observations by the CRRES and GOES spacecraft indicated that a power law field line variation with  $p = 2$  does a good job of modeling the average field line dependence of mass density (at high altitudes above at least  $1 R_E$ ) for  $L = 4 - 5$ ,  $p = 1$  is best for  $L = 5 - 6$ , and at larger  $L$  shells there may be an equatorial peak in mass density (nonmonotonic variation between the magnetic equator and the ionosphere) that is largest in the afternoon local time sector at geomagnetically active times (Takahashi et al. 2004; Denton et al. 2002b; Denton 2006). There is evidence from ground-based observations that a larger value of  $p$  might be applicable to lower  $L$  shells where ionospheric mass loading has a larger effect (Menk et al. 1999; Price et al. 1999; Denton 2006).

Recently, Denton et al. (2009) were able to measure with unprecedented precision the Alfvén wave frequencies of eight harmonics observed by the CLUSTER 1 spacecraft at perigee ( $L = 4.8$ ). Using a polynomial expansion for the field line dependence as a function of a coordinate related to  $\lambda$ , they inferred the field line dependence for mass density shown in Fig. 1. The field line dependence is very flat ( $p \approx 1$ ) out to  $|\lambda| = 30^\circ$ , but increases steeply as  $|\lambda|$  increases. As Denton et al. (2009) showed, the large mass density inferred at low altitude (large  $|\lambda|$ ) is consistent with values from the International Reference Ionosphere (IRI) model (Bilitza 2001). Because the inferred mass density is so large near the ionosphere, the portion of the field line near the ionosphere makes a difference in the Alfvén wave frequency. That is, the Alfvén wave frequency is not merely dependent on the mass density in the equatorial region of the field line.

### 3.3 Event-Driven Density Model

Denton et al. (2006a) constructed an event-driven model of magnetospheric density for 29 August 2000 using data from IMAGE and ground magnetometers. A map of the plasmapause position was determined from a two-dimensional image of the plasmasphere taken by the EUV instrument on IMAGE using the method of Goldstein et al. (2003). The radial dependence of the electron density in the plasmasphere was determined from in situ electron density measurements from the passive radio wave emissions observed by the IMAGE RPI instrument (Benson et al. 2004). The MLT dependence of the plasmaspheric density was determined from the inferred “pseudodensity” found by inverting the EUV emissions

**Fig. 2** **a** IMAGE EUV image of resonantly scattered solar EUV photons (30.4 nm) at 29 August 2000 at 15:19 UT. **b** Simulated EUV image using the model for electron density developed in Denton et al. (2006a). (Adapted from Denton et al. 2006a)



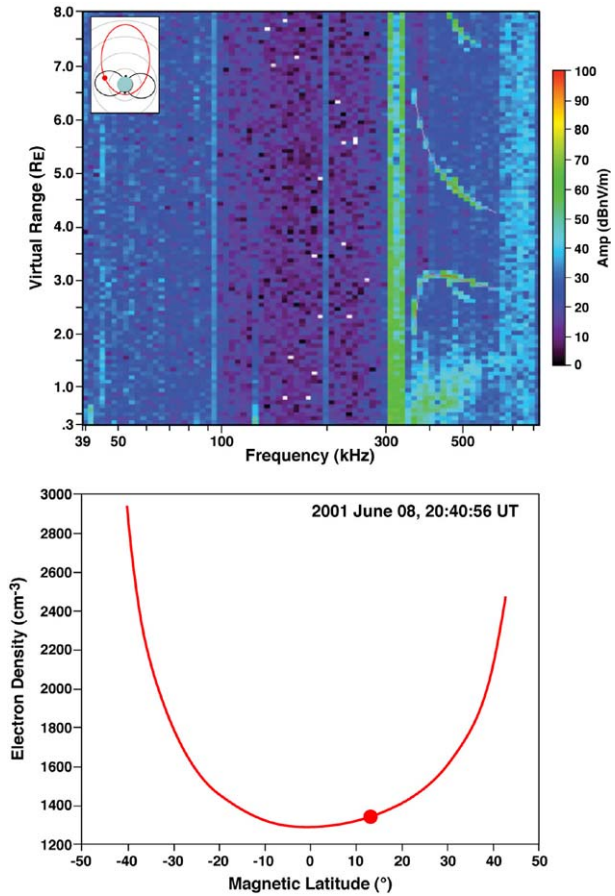
(Gallagher et al. 2005). (In principle, one could use such a pseudodensity to get all the information about the distribution; but in practice, it is better to use all the information available, including the in situ data.) The radial dependence of the density outside the plasmapause in the afternoon local time sector was determined from the inferred mass density based on toroidal Alfvén wave frequencies observed by ground magnetometers (Waters et al. 2006). The field line dependence model of Denton et al. (2002b) was used to extend the equatorial density into a three dimensional distribution and the Gallagher et al. (2000) model was used in the polar cap. Figure 2 shows (a) the EUV image, and (b) a simulated EUV image using the model.

### 3.4 Field-Aligned Dependence from IMAGE RPI Measurements

RPI onboard IMAGE used the radio sounding technique to remotely measure the electron density in the magnetosphere (Reinisch et al. 2000). The instrument, in active sounding modes, transmitted coded signals with frequencies sweeping from 3 kHz to 3 MHz and listened to the echoes. The received signals are plotted in the form of the plasmagram, a color-coded display of signal amplitude as function of frequency and echo delay time (Galkin et al. 2004). Echoes that experienced the same dispersion during the propagation form a distinct trace in the plasmagram. Under certain conditions (see Reinisch et al. 2001b; Fung et al. 2003; Green and Reinisch 2003; Fung and Green 2005), the echo traces represent the reflected signals that propagated along a magnetic field line threading the satellite. By scaling the traces in a plasmagram and using a new density inversion algorithm, which is based on the ionospheric density inversion technique of Huang and Reinisch (1982), an almost instantaneous (in less than 1 minute) density distribution can be derived along a field line from a single plasmagram. This new algorithm has been discussed in detail in a number of previous publications (Reinisch et al. 2001a, 2001b; Huang et al. 2004; Song et al. 2004). Figure 3 displays, as an example, a plasmagram obtained by RPI in the plasmasphere showing multiple traces (top panel) and the field-aligned electron density profile (bottom panel) derived from the traces shown in the plasmagram. Such true field-aligned density profiles are available only after the launch of the IMAGE satellite. Those electron density distributions provide the most accurate representation of the field-line dependence of the electron density because the multiple point (20 to over 100) measurements were made almost instantaneously ( $\leq 1$  minute) along the individual field lines by RPI (Huang et al. 2004; Reinisch et al. 2001a, 2001b, 2004; Song et al. 2004).

RPI recorded over one million plasmagrams in the plasmasphere, trough, and polar cap. The density inversion technique has been applied to process plasmagrams with echo traces of good quality. The sequence of field-aligned density profiles obtained during one satellite pass allows the construction of the 2-dimensional (2-D) electron density distribution in the

**Fig. 3** (Top) Plasmagram recorded inside the plasmasphere displaying the echo amplitude as function of frequency and virtual range. The insert shows the orbit (red line) and location (red square) of IMAGE at the time of the sounding. The field lines of  $L = 4$  are shown in black lines. (Bottom) The density profile, as function of magnetic latitude, inverted from the plasmagram shown in top panel. (Adapted from Huang et al. 2004)



plane containing the field lines and the orbit. Figure 4 shows such 2-D distributions projected onto the solar magnetic (SM)  $X_{SM}-Z_{SM}$  plane. These density images span the regions of the polar cap, cusp/dayside auroral oval, trough, and the plasmasphere.

With such 2-D density distributions it is possible to construct an empirical model showing the global density distribution in the near-Earth magnetosphere. Huang et al. (2004) has demonstrated, as the first step, the possibility to derive a 2-D plasmaspheric density model. Huang et al. (2004) used seven consecutive density profiles inverted from the RPI sounding measurements, when IMAGE passed through the plasmasphere from  $L = 3.23$  to  $L = 2.22$  on the morning side on 8 June 2001. Figure 5 displays those field-aligned density profiles. Huang et al. (2004) demonstrated that those density profiles can be well represented by a single functional form as given by

$$n_e(L, \lambda) = n_{e0}(L) \left( 1 + \gamma \frac{\lambda}{\lambda_{inv}} \right) \sec^{\beta(L)} \left( \frac{\pi}{2} \frac{\alpha \lambda}{\lambda_{inv}} \right),$$

$$n_{e0}(L) = A(B/L - 1),$$

$$\beta(L) = C + D \cdot L,$$
(7)

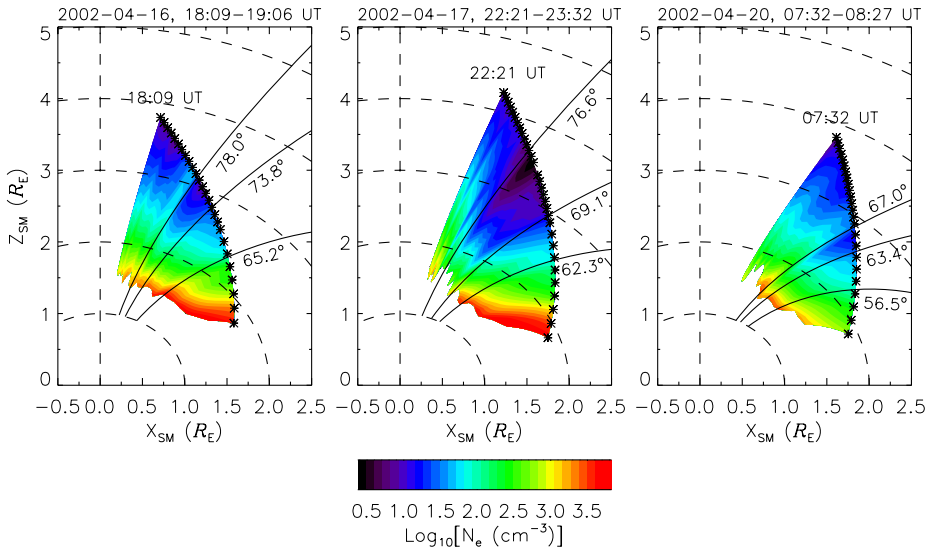


**Fig. 4** Two-dimensional (2-D) electron density ( $n_e$ ) images projected onto the solar magnetic (SM)  $X_{SM}$ - $Z_{SM}$  plane. The 2-D images are derived from the field-aligned density profiles measured by RPI from 18:09 to 19:06 UT on 16 April 2002, 22:21 to 23:32 UT on 17 April 2002, and 07:32 to 08:27 UT on 20 April 2002, respectively. The stars on each orbit segment indicate the locations from which the field-aligned density profiles were measured. Also plotted are three field lines (solid) with the corrected geomagnetic coordinate (CGM) latitude labeled. The field line of lowest latitude indicates the plasmapause, while the other two field lines delimit the density depletion region in each panel. (Adapted from Tu et al. 2005b)

where  $n_{e0}(L)$  is the equatorial density,  $\gamma$  describes the asymmetry of the north-south distribution around the equator with  $\gamma < 0$  ( $\gamma > 0$ ) corresponding to higher density in the southern (northern) hemisphere than at conjugate points in the northern (southern) hemisphere, the power index  $\beta(L)$  defines the steepness of the profile at high latitudes, and  $\alpha$  specifies the flatness of the profile at low latitudes. The  $A$ ,  $B$ ,  $C$ ,  $D$ ,  $\gamma$ , and  $\alpha$  are fitting parameters. Their values are determined by applying a multi-variant least square fit of (7) to the multiple density profiles. The multi-variant least square fit requires that the square sum of the difference between the measured and modeled electron densities is minimized with respect to six common fitting parameters if using (7), or five fitting parameters if using the functional form modified by Tu et al. (2006) (see (10))

$$\Delta = \sum_i \sum_j [n_{ij}^* - n_{ij}]^2 = \min, \tag{8}$$

where  $i$  and  $j$  represent the  $i$ th field line and the  $j$ th point on the  $i$ th field line, respectively, and  $n_{ij}^*$  and  $n_{ij}$  are the measured and modeled electron density, respectively. For the morning sector case on 8 June 2001 shown in Fig. 5,  $A = 4833 \text{ cm}^{-3}$ ,  $B = 3.64$ ,  $C = 0.2$ ,  $D = 0.03$ ,  $\gamma = -0.14$ , and  $\alpha = 1.25$ . The fitted density profiles are superimposed on the measured density profiles in Fig. 5 as red dashed lines. With the values of the fitting parameters specified, a 2-D plasmasphere density image can be determined from (7) as shown in Fig. 6. It should be pointed out that the equatorial densities shown as measured in Fig. 5 are in fact generally interpolations from observations. RPI soundings only return echoes from regions with densities higher than that at the spacecraft location. Off-equatorial spacecraft passage through a given  $L$ -shell therefore results in a gap in remotely observable electron

**Fig. 5** Density profiles on 8 June 2001. The *solid black lines* are inverted from measurements, and the *red dashed lines* are the empirical model. (Adapted from Huang et al. 2004)

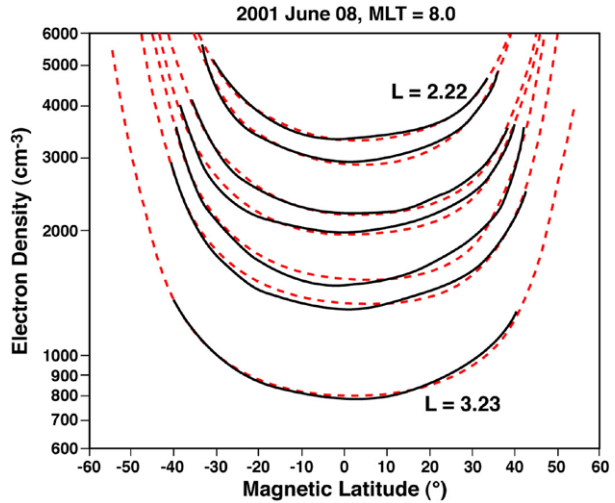
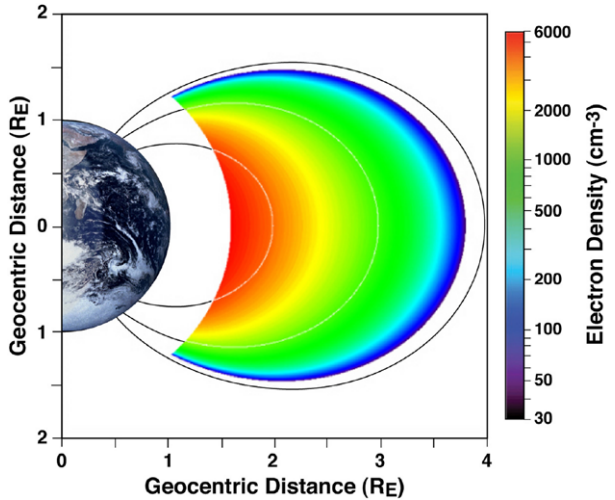


**Fig. 6** Empirical model for the 8 June 2001 event at MLT = 8 hours. (Adapted from Huang et al. 2004)



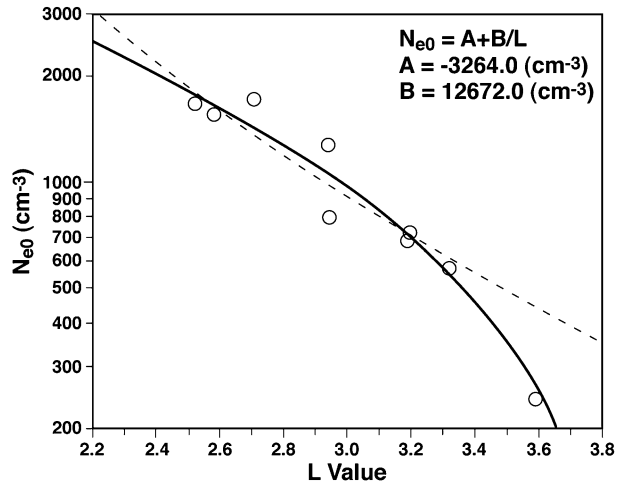
densities at lower magnetic latitudes. Echoes are returned to the spacecraft from both sides of this low latitude region, enabling the direct derivation of densities at higher latitudes in both hemispheres.

In a study of plasmasphere depleting and refilling, Reinisch et al. (2004) applied a similar technique to fit the multiple density profiles obtained by RPI in the noon sector before a great magnetic storm on 31 March–2 April 2001. From the best fit to nine density profiles, the equatorial electron density as a function of  $L$  is derived as

$$n_{e0}(L) = 3264(3.88/L - 1). \tag{9}$$

The plasmapause is inferred to be within but near  $L = 3.88$  where the model (9) predicts the plasma density to be zero. This function for the equatorial density is plotted as a solid line in Fig. 7. The dashed line depicts the  $L^{-4}$  dependence expected for total electron density conservation as flux tubes move radially. Either fit is appropriate in the range from  $L = 2.5$

**Fig. 7** The equatorial plasma density as a function of  $L$ -value from the measurements near 12:00 MLT (open circles) before the storm event. The solid line shows the best fit hyperbolic function. The dashed line is the best fit  $L^{-4}$  function as predicted by the conservation of magnetic volume. (Adapted from Reinisch et al. 2004)

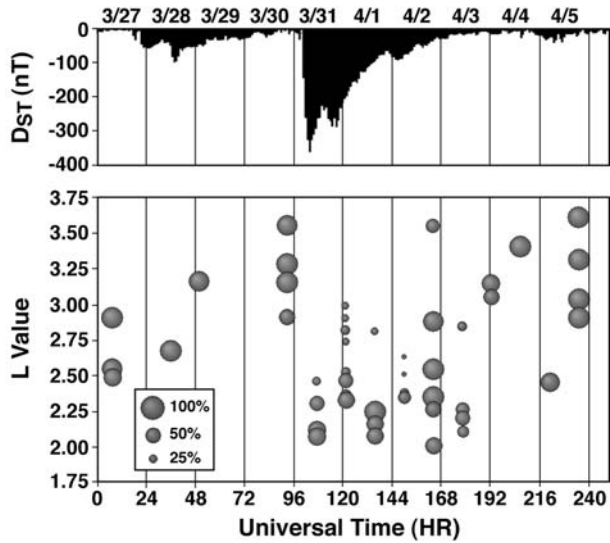


to 3.4, however a significant difference occurs at larger  $L$  value between the  $L^{-4}$  function and the measured equatorial density.

The modeled equatorial densities (quiet time values) were then used as the reference to assess the plasmasphere depletion and refilling during the course of the magnetic storm. The top panel of Fig. 8 shows the progress of the storm in  $Dst$ . The storm started near 06:00 UT, on 31 March 2001 (102 hours in Fig. 8 that starts at 00:00 UT on 27 March 2001), and lasted for about 30 hours. The positions of the “spheres” in the lower panel of Fig. 8 show the  $L$ -values and times when the measurements were made. Each column of spheres in the lower panel corresponds to an orbital pass, which occurs every 14.2 hours. To examine the time evolution of the plasma density, the filling ratio is defined as the ratio of the measured equatorial density to the quiet time value calculated from (9) at the same  $L$ -value. The size of the sphere in the lower panel of Fig. 8 is proportional to this filling ratio as shown in the legend. Depletion was observed during the storm in the region where  $L \geq 2.2$ , indicating that the plasmapause moves from  $L \geq 3.6$  before the storm to  $L \approx 2.2$  during the storm, as shown in lower panel of Fig. 8 after 102 hours. There is apparent refilling of the flux tubes with  $L \leq 3$  observed at 20:30 UT on 2 April 2001, which was most likely due to corotating spatial structures (plasmaspheric plume) as suggested by correlating the global images of the plasmasphere from the IMAGE EUV with the RPI observations in the noon sector (Reinisch et al. 2004). The refilling start time cannot be accurately determined because of the 14.2-hour orbit period of the IMAGE spacecraft. However, from the still depleted flux tubes observed at 11:30 UT on 3 April and completely refilled flux tubes at 18:00 UT on 4 April 2001, the refilling time scale is estimated to be less than 31 hours, which is much shorter than that predicted by the theories at those  $L$  values (e.g., Singh and Horwitz 1992, and references therein).

Tu et al. (2006) extended this technique to model the RPI density profiles acquired near 00:00 MLT for both plasmasphere and trough. In the study of Tu et al. (2006) the parameter  $\alpha$  in (7) is  $L$ -value dependent, while the north-south asymmetry of the density profiles is ignored ( $\gamma = 0$ ). The  $L$  dependence of  $\alpha$  is to account for the different slopes of the profiles in the inner plasmasphere, outer plasmasphere and trough. The modified functional form (based on Tu et al. 2006, (1)) is written as

**Fig. 8** Time history of the *Dst* index (*top*), and the filling ratio as function of *L* value and time (*bottom*). The size (area) of the circles in the *bottom panel* is proportional to the filling ratio. The filling ratio is defined as the measured equatorial density normalized by its quiet time value. (Adapted from Reinisch et al. 2004)



$$n_e(L, \lambda) = n_{e0}(L) \sec^{\beta(L)} \left( \frac{\pi}{2} \frac{\alpha(L)\lambda}{\lambda_{inv}} \right),$$

$$\alpha(L) = A + B \cdot L, \tag{10}$$

$$\beta(L) = C + D \cdot L,$$

where the equatorial density  $n_{e0}(L)$  cannot be obtained from the observed density profiles, particularly those in the outer plasmasphere or trough, because they cover only one hemisphere (either northern or southern).  $n_{e0}(L)$  is a fitting parameter as are the  $A$ ,  $B$ ,  $C$ , and  $D$ . Three IMAGE passes near the midnight plasmasphere/trough were selected. Along each pass multiple density profiles were inverted from the RPI sounding measurements. The multivariate least square fitting was then applied to the density profiles for each pass using (10).

Shown in Fig. 9 are the observed (solid lines) and fitted (dashed lines) density profiles for three passes corresponding to a storm recovery phase, a prolonged quiet period, and a storm sudden commencement, respectively, from left to right. It is seen from Fig. 9 that in each pass the density profiles along the filled (in the inner plasmasphere) and the depleted (in the outer plasmasphere or trough) flux tubes can be well modeled with the above functional form (the relative error between the modeled and observed densities is <6%). In each panel of Fig. 9 different sets of the values for the fitting parameters,  $A$ ,  $B$ ,  $C$ , and  $D$ , have been used for filled and depleted flux tubes in order to get good fits for two groups of density profiles (Tu et al. 2006). For the three passes examined, the fitting parameter values are not sensitive to the geomagnetic activity for the inner plasmasphere density profiles but vary slightly for the trough density profiles from case to case. The cases examined suggest that there are two different field line dependences of the field-aligned density profiles in the inner filled plasmasphere and trough or depleted outer plasmasphere with steeper density slopes in the latter region.

The equatorial densities  $n_{e0}(L)$  from the best fits to the measured density profiles in each case are the extrapolation of the density profiles to the equator, where there were no RPI observations for the three cases. Figure 10 displays the extrapolated equatorial density as a function of  $L$  for three cases shown in Fig. 9. The extrapolated equatorial density in the

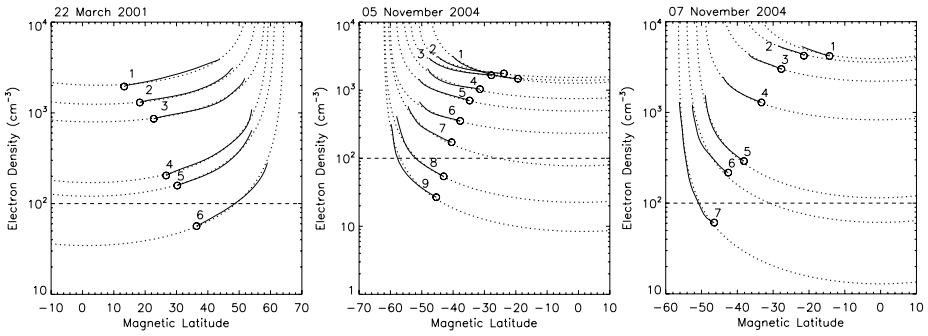


**Fig. 9** Field-aligned electron density profiles derived from the RPI sounding measurements made from 01:19–01:43 UT on 22 March 2001 (left panel); from 05:33–05:57 UT on 4 November 2004 (middle panel); from 14:17–14:35 UT on 7 November 2004 (right panel). The circle on each profile indicates the satellite location. The profile number is labeled beside each profile. The dotted lines are the multi-variant least square fits to the measured density profiles using (7). The horizontal line on each panel represents density level of  $100 \text{ cm}^{-3}$ . (Adapted from Tu et al. 2006)

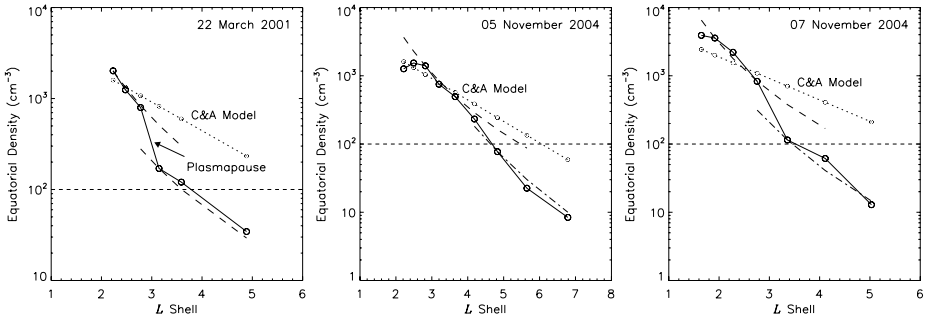


**Fig. 10** Equatorial density (solid line with open circles) extrapolated from the multi-variant least square fits to the measured density profiles for the 22 March 2001 case (left panel), the 5 November 2004 case (middle panel), and the 7 November 2004 case (right panel). In all panels, the dashed line corresponds to a  $L^{-4}$  dependence of the equatorial density, while the dotted line with filled circles is the filled plasmasphere equatorial density from the Carpenter and Anderson (1992) model. The dashed-dotted line in the middle (right) panel corresponds to a  $L^{-6}$  ( $L^{-5.1}$ ) dependence of the equatorial density. The horizontal line on each panel represents density level of  $100 \text{ cm}^{-3}$ . (Adapted from Tu et al. 2006)

filled flux tubes (in the inner plasmasphere) decreases as  $L^{-4}$  (except for the complicated density structure in the 5 November 2004 case), faster than that predicated by the empirical model of Carpenter and Anderson (1992) but consistent with that in the observations of Reinisch et al. (2004). The plasma trough equatorial density (lower three profiles in Fig. 9 for the 22 March 2001 case) also varies with  $L^{-4}$ , slightly slower than that predicted by Carpenter and Anderson model ( $n_{e0} \propto L^{-4.5}$ ) but the same as that in the model of Sheeley et al. (2001) and in the observations of Denton et al. (2004). The extrapolated equatorial density of the depleted flux tubes in the outer plasmasphere (lower three profiles in Fig. 9 for the other two days), however, decreases with  $L$  much faster, approximately  $\propto L^{-\gamma}$  with  $\gamma \geq 5$ . The difference in the  $L$  dependence between the extrapolated equatorial density and the empirical model of Carpenter and Anderson (1992) may be explained by fluctuations of the individual case observations from the average.

Due to the good fits of the functional form in (7) (or (10)) to the RPI density profiles observed in morning, noon, and midnight sectors, it is reasonable to suggest that the functional form has the potential to be used for constructing global plasmasphere/plasma trough models. Particularly, it is feasible to be used to specify the density profiles along the nightside depleted flux tubes for the studies of plasmasphere refilling with appropriately specified fitting parameter values and equatorial densities.

#### 4 Field-Aligned Density Distributions in the Polar Cap

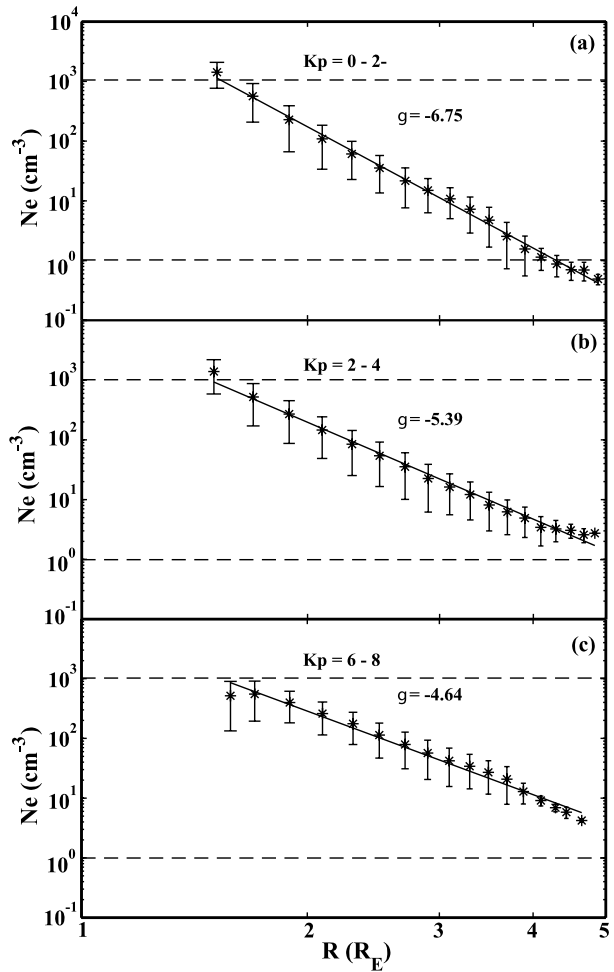
Plasma density distributions in the polar cap (above altitude of 3000 km) have been investigated using the in situ measurements from the S3-3, DE-1 and POLAR, missions (e.g., Mozer et al. 1979; Persoon et al. 1983; Gallagher et al. 2000; Johnson et al. 2001, 2003). Those previous studies established that the statistical dependence of the polar cap density on radial distance follows a power law and revealed the significant effects of solar illumination on polar cap density distributions. Other factors, such as geomagnetic activity, have not been incorporated into the empirical models of polar cap densities.

In a single IMAGE pass, the RPI remote sounding provided multiple measurements that are equivalent to in situ measurements of many passes. Along individual field-aligned density profiles there are typically over 30 density measurements. Therefore, RPI collected a very large number of density measurements during its 5.8-year operation. More importantly, the field-aligned density profiles contain the information of the field-line dependence that allows better statistical description of the density distributions. Using such RPI density profiles, Nsumei et al. (2003) constructed an empirical model for polar cap densities, which has a power law with an exponent of  $-5.09 \pm 0.03$ . Furthermore, this model includes dependence on geomagnetic activity as measured by the 3-hour  $K_p$  index. The Nsumei et al. (2003) model was developed by using a small database covering the period from June to November 2001.

With a much larger database consisting of 770 RPI density profiles, Nsumei et al. (2008) further developed a polar cap density model. In their study, the relative importance of solar illumination and geomagnetic activity dependences of electron densities in the polar cap was systematically examined. This statistical analysis considered the dynamic nature of the size and shape of the polar cap by using a statistical poleward boundary model of the auroral oval developed by Carbary (2005). The modeled poleward boundary depends on MLT and the  $K_p$  index. RPI measurements at invariant latitudes greater than this poleward auroral boundary are designated as polar cap. Such a definition of the polar cap largely avoids contaminations by auroral oval and sub-auroral region density measurements.

The statistical analysis of the RPI electron density distributions not only shows that the electron density distribution within the polar cap depends on the geocentric distance  $R$  and geomagnetic activity level, but also reveals that the enhancement of the electron density during periods of increased geomagnetic activity is altitude dependent such that it is most pronounced at higher altitudes and less significant at lower altitudes. The density increase with increasing  $K_p$  value can be seen from a comparison of the three panels (for three different  $K_p$  ranges) in Fig. 11. The similar density at lower altitudes and different densities at higher altitudes suggest non-local outflow and/or convection across the polar cap associated with changes in geomagnetic activity, particularly at high altitudes. On the other hand, the strong solar illumination control of electron density at lower altitudes, but not at higher, is demonstrated by Fig. 12. It is clear that electron density is higher on the sunlit side than on the dark side. The enhancement in electron density due to solar illumination decreases with

**Fig. 11** Log-log plot of average electron density  $n_e$ , versus geocentric distance  $R$ , in three geomagnetic activity ranges. The RPI data are divided into  $0.3 R_E$  bins in geocentric distances and three  $K_p$  ranges. The average electron density is computed for each bin. At higher altitudes, the electron density increases more significantly with geomagnetic activity levels measured by the  $K_p$  index. The two horizontal lines on each panel represent density level of 1 and  $10^3 \text{ cm}^{-3}$ , respectively. (Adapted from Nsumei et al. 2008)



increasing altitude. These results are similar to those of Johnson et al. (2003) and indicate decreasing/increasing importance of the solar zenith angle/cleft ion fountain on density with increasing altitude (Tu et al. 2005a).

Based on a statistical analysis of the RPI database, Nsumei et al. (2008) obtained an empirical representation of polar cap densities

$$\begin{aligned}
 n_e(r, K_p, \chi) &= n_{e0}(K_p, \chi) \left(\frac{r}{r_0}\right)^{g(K_p, \chi)}, \\
 n_{e0}(K_p, \chi) &= n_{e00} \exp(\alpha_1 K_p + \alpha_2 \cos \chi), \\
 g(K_p, \chi) &= \gamma_0 + \gamma_1 K_p + \gamma_2 \chi,
 \end{aligned}
 \tag{11}$$

where  $r_0 = 1.4 R_E$  and  $\chi$  is the solar zenith angle (in degrees) at 300 km altitude of the field line. The coefficients in (11), determined by a multivariate fit of RPI data to the above expressions, are given by:  $n_{e00} = 7.29 \times 10^2 \text{ cm}^{-3}$ ;  $\alpha_1 = 0.0747$ ;  $\alpha_2 = 1.8959$ ;  $\gamma_0 = -8.6400$ ;  $\gamma_1 = 0.2601$ ;  $\gamma_2 = 0.0261$ . It is interesting to note that  $\chi$  is a function of UT, local time (LT),

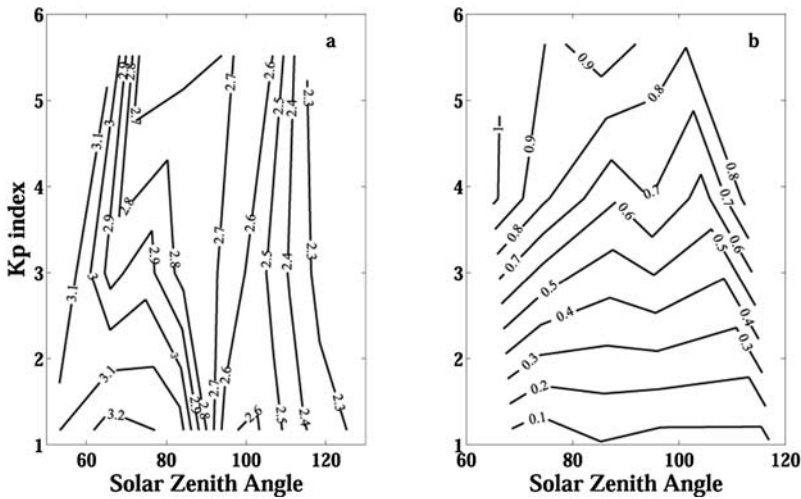


**Fig. 12** Contours of the logarithm of average electron density ( $\text{cm}^{-3}$ ) are shown as functions of solar zenith angle and the geomagnetic activity index  $K_p$  for two altitude ranges: **a**  $R = 1.4 - 1.7 R_E$ , **b**  $R = 4.0 - 4.4 R_E$ . (Adapted from Nsumei et al. 2008)

and latitude. Thus the present empirical model also has dependence on UT, LT, and latitude. Equation (11) was developed from measurements covering geocentric distances from  $1.4 R_E$  to a little over  $4.5 R_E$ , geomagnetic activity from  $K_p = 0$  to almost  $K_p = 6$ , and for solar zenith angles ranging from roughly 70 degrees to 110 degrees. In this study only  $K_p$  was used to roughly characterize the noted increase in higher altitude densities with increased activity. Future studies might more directly consider solar wind drivers, such as that found by Moore et al. (1999), where ionospheric high-latitude outflow was found to be correlated with solar wind dynamic pressure.

### 5 Empirical Models of Electric Field

#### 5.1 The Corotation Electric Field

Close to the Earth, the main source of the magnetospheric electric field is the corotation electric field due to rotation of the Earth along its axis. In the equatorial plane, the potential of the co-rotation electric potential is given by (e.g., Kivelson and Russell 1995)

$$\Phi = -\frac{\omega R_E^2 B_0}{r/R_E} = -\frac{92}{r/R_E} \text{ [kV]}, \tag{12}$$

where  $\omega = 7.272 \times 10^{-5} \text{ s}^{-1}$  is the angular rotation frequency of the Earth,  $r$  is the radial distance,  $R_E = 6371 \text{ km}$  is the Earth radius and  $B_0 = 3.1 \times 10^{-5} \text{ T}$  is the magnetic field strength at the surface of the Earth at the equator.

#### 5.2 Empirical Convection Electric Field Models

The other large-scale source of magnetospheric electric field is the convection electric field, controlled by the solar wind conditions and the level of geomagnetic activity. To determine the global electric field distribution in the whole magnetosphere, various empirical

and mathematical models have been built with various degrees of sophistication. Reviews of convection electric fields were presented in Stern (1977), Lyons and Williams (1984), del Pozo and Blanc (1994), and Ebihara and Ejiri (2002) for instance. The electric field models are empirical or based on the solutions of physical equations, exactly like plasmaspheric models (Pierrard et al. 2008b). Semi-empirical models have also been developed by the pioneer researchers (Nishida 1966), and later the model of Sojka et al. (1986) that is dependent on  $K_p$  and on the IMF intensity and direction. We give here first a short overview of empirical electric field models recently used in plasmaspheric research, including a newly developed inner magnetospheric electric field (UNH-IMEF) model using CLUSTER data. Then we discuss the influence of the empirical models on the investigations of plasmaspheric dynamics and plasmopause formation.

5.2.1 Volland-Stern’s and Maynard-Chen’s (VSMC) Convection Electric Field Model

The Volland-Stern model (Volland 1973; Stern 1975) is a simple mathematical model where a uniform dawn-dusk convection electric potential distribution is applied across the magnetosphere. This magnetospheric electric field derives from a scalar potential which, in a co-rotating frame of reference, is given by

$$\Phi = Ar^2 \sin \phi, \tag{13}$$

where  $\phi$  is the azimuthal angle from noon and the  $K_p$  dependent factor

$$A = \frac{0.045}{(1 - 0.159K_p + 0.0093K_p^2)^3} \text{ [kV}/R_E^2] \tag{14}$$

determines the convection electric field intensity. The  $K_p$  dependence of this empirical model was obtained by Maynard and Chen (1975) by adjusting the last closed equipotential (LCE) of the total electric field in order to favorably compare with plasmopause positions determined by OGO3 and OGO5 satellite observations; this model has been given the acronym VSMC in the following.

5.2.2 McIlwain’s E5D Convection Electric Field Model

Another analytical representation of the magnetospheric convection electric potential was derived by McIlwain (1986) from electron and proton dynamical spectra measured at geosynchronous orbit during the ATS-5 and ATS-6 missions. This potential is given by

$$\Phi = [r(0.8 \sin \phi + 0.2 \cos \phi) + 3] \left[ 1 + 0.3 \frac{K_p}{1 + 0.1K_p} \right] \left[ \frac{1}{1 + (0.8R_{ar}/r)^8} \right], \tag{15}$$

where  $R_{ar} = 9.8 - 1.4 \cos \phi - (0.9 + 0.3 \cos \phi)[K_p/(1 + 0.1K_p)]$ .

The E5D model depends also on the three-hourly geomagnetic activity index  $K_p$ . The E5D model was deduced from ATS-5 and ATS-6 particle flux measurements at geosynchronous altitude. The E5D model was derived by fitting the observed positions of the injection boundary.

Figure 13 illustrates the equatorial contour maps of the equipotentials for the VSMC and E5D convection electric field models for  $K_p = 6$ . The models are quite different from each other. The comparison of Fig. 13 indicates that the E5D electric field model is less sensitive to  $K_p$  than the VSMC model. The LCE is everywhere closer to the Earth for the VSMC model than for the E5D one.

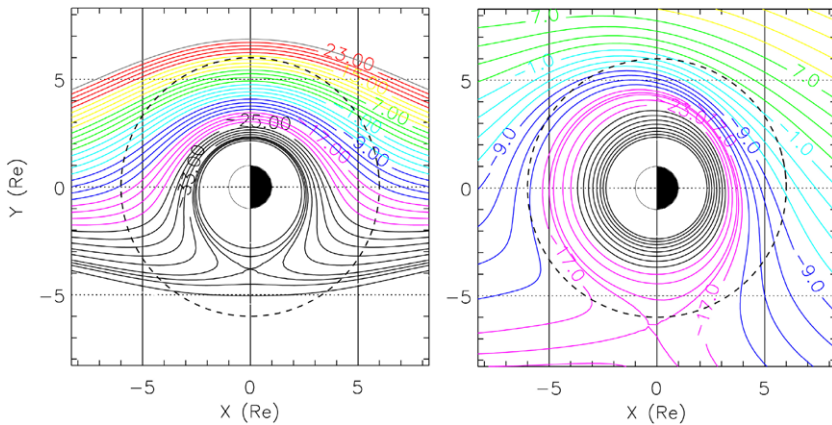


**Fig. 13** Equipotential map of the total electric field including convection model and corotation for  $K_p = 6$ : VSMC (left panel) and E5D (right panel). The values of the potential (in kV) are given on the equipotential contours, which are drawn every 2 kV. The dotted circle corresponds to  $L = 6$ . (Adapted from Pierrard et al. 2008a)

### 5.2.3 Weimer’s Convection Electric Field Model

Unlike the two previous electric field models, Weimer’s (Weimer 1996) electric field model is driven by solar wind parameters: IMF magnitude, solar wind velocity, and dipole tilt angle. It was derived from low altitude ionospheric convection velocity measurements at high latitudes. The electric potential in the Weimer (1996) model,  $\Phi$ , is given by an expansion in spherical harmonics as a function of the geomagnetic co-latitude  $\theta$ , the MLT  $\phi$ , and associated Legendre functions  $P_l^m$

$$\Phi(\theta, \phi) = \sum_{l=0}^{\min(l,3)} (A_{lm} \cos m\phi + B_{lm} \sin m\phi) P_l^m(\cos \theta). \tag{16}$$

The  $A_{lm}$  and  $B_{lm}$  coefficients were derived by a least error fit from multiple satellite measurements of the ionospheric convection velocity.

Figure 14 illustrates the equatorial contour maps of Weimer’s convection electric potential including corotation every UT hour from 07:00 UT up to 12:00 UT during the geomagnetic event of 17 April 2002. The LCE has a stagnation point at 18:00 MLT in the dusk sector for VSMC and E5D models, while it is generally located at later MLT, in the post-dusk local time sector, for Weimer’s model. Weimer’s equipotentials are quite different from those of the E5D and VSMC for the same period. The shielding is often less efficient in the dawn sector than at dusk unlike in E5D. The electric field intensity of the Weimer model is also generally found to be stronger than that of either the E5D or VSMC during geomagnetic storms and substorms.

Other sophisticated ionospheric and magnetospheric electric field models are also available in the literature (Richmond and Kamide 1988; Boonsirirath et al. 2001). These convection electric field models have been compared with observations to study the effects of inner magnetospheric convection on ring current dynamics (Jordanova et al. 2001) and on stormtime particle energization (Khazanov et al. 2004).

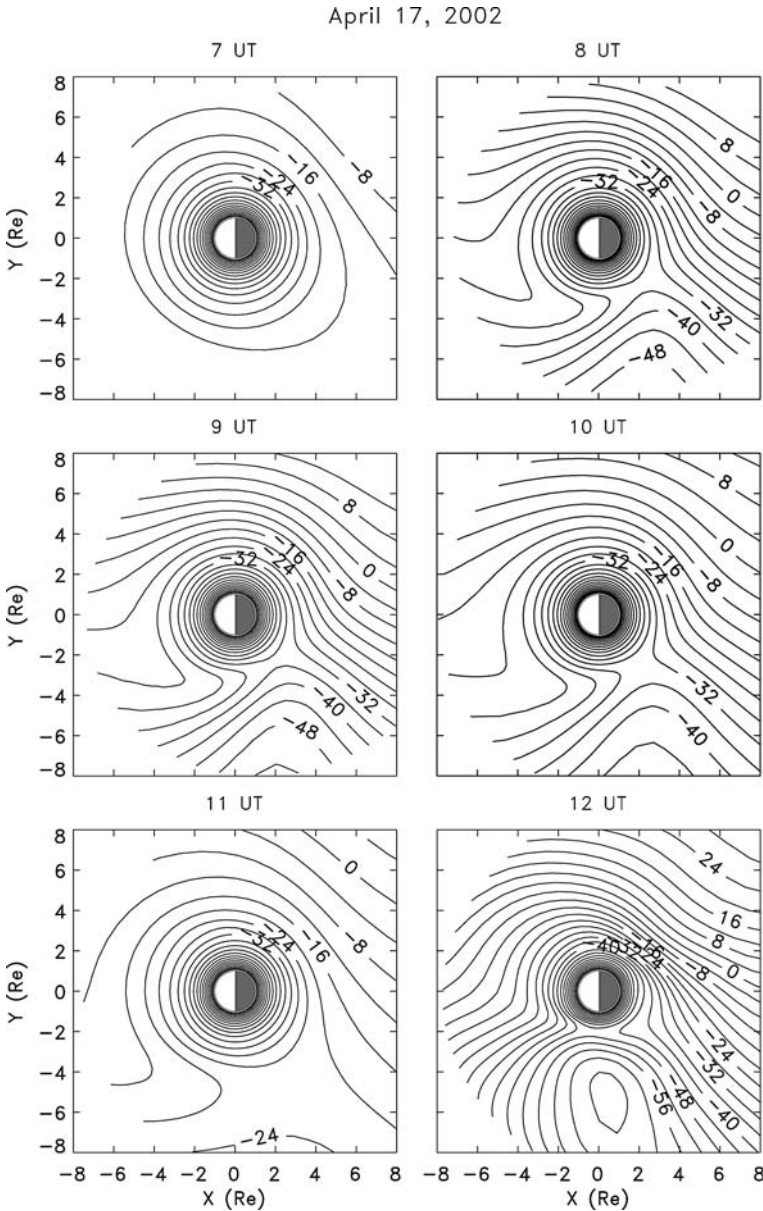
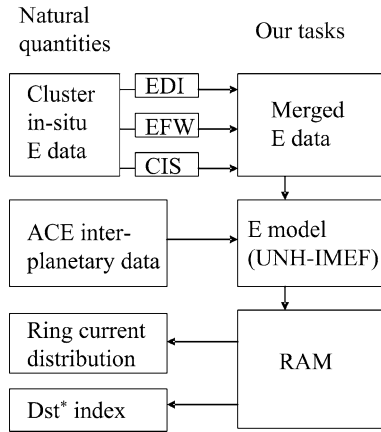


**Fig. 14** Equipotential map of the Weimer convection electric field dependent on solar wind conditions on 17 April 2002 with corotation electric field. T96 magnetospheric magnetic field model (Tsyganenko and Stern 1996) is used to map electric potential from the ionospheric altitude to the equator. The values of the potential (in kV) are given on the equipotential contours, which are drawn every 4 kV

*5.2.4 Inner Magnetospheric Electric Field (UNH-IMEF) Model*

Most of electric field models mentioned above have been developed using measurements at ionospheric altitudes. The application of such models to magnetospheric altitudes strongly

**Fig. 15** A block diagram to show the work to be performed. Data set is shown on the *left*, while tasks are shown on the *right*



relies on the assumption that magnetic field lines are equipotentials. This assumption, however, may be violated in regions where field-aligned currents exist and during periods of geomagnetic disturbances. It is thus important to derive an electric field model from in situ measurements made closer to the magnetic equator in the inner magnetosphere in order to mitigate the influence of the field-aligned potentials.

The Electric Drift Instrument (EDI) on each of three CLUSTER satellites provides an excellent opportunity to derive empirical electric field models at higher altitudes. EDI measures particle drift motion, which mostly consists of  $\mathbf{E} \times \mathbf{B}$  drift (Paschmann et al. 2001). Matsui et al. (2004) have conducted a statistical study using two years of EDI data obtained in the inner magnetosphere. In that study, electric potential patterns were derived from the average electric field by solving an inverse problem. The statistical data were organized with the southward component of the IMF ( $B_z$ ), the  $K_p$  index, and the  $Dst$  index. The derived patterns, however, contained significant statistical errors because of the small database and possibly also due to a data coverage gap corresponding to the nightside MLT.

In order to reduce statistical errors and provide a better description of electric fields in the inner magnetosphere, the merging of over 5 years-worth of EDI measurements with electric field measurements from three other CLUSTER instruments has been proposed (Puhl-Quinn et al. 2008; Matsui et al. 2008). Those instruments are the Electric Field and Wave (EFW) instrument (Gustafsson et al. 2001), the Cluster Ion Spectrometry (CIS) instrument (Rème et al. 2001), and the FluxGate Magnetometer (FGM) instrument (Balogh et al. 2001). EFW is a conventional instrument for measuring electric fields that uses double probes. CIS provides three-dimensional ion distribution functions from which it is possible to calculate the bulk velocity of ions,  $\mathbf{V}$ . Using the magnetic field,  $\mathbf{B}$ , as measured by FGM, electric fields can be calculated by  $\mathbf{E} = -\mathbf{V} \times \mathbf{B}$ . These three types of electric field data will be merged into a single database in order to maximize data coverage. Only the highest quality data will be kept. Figure 15 is a block diagram showing the data sets used to create the database, and the tasks that have been (or will be) performed using the database. The data sets used (or produced) are shown on the left, while tasks are shown on the right.

In order to develop a merged database, Puhl-Quinn et al. (2008) compared EDI and EFW data in three orbits near the magnetic equator (Fig. 16). Electric field data from EDI are shown in black, while that from EFW are shown in red. The electric field component shown in the figure is the  $X$  component in the  $X$ - $Y$  plane of the despun-satellite-inverted (DSI) coordinates, which are similar to geocentric solar ecliptic (GSE) coordinates. The spacecraft

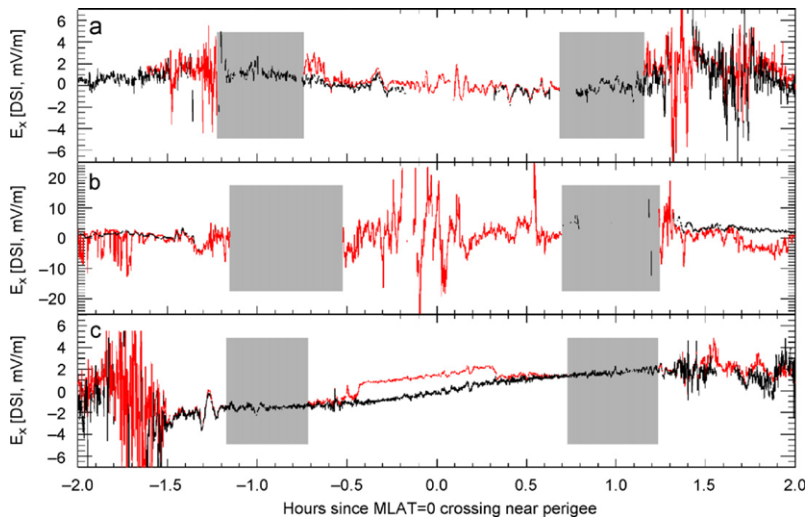


**Fig. 16** Comparison of electric fields from EDI (black) and EFW (red).  $X$  component of electric field in despun satellite inverted (DSI) coordinates is shown near magnetic equator for three orbits: **a** 2 October 2001, **b** 18 April 2002, and **c** 4 July 2001. Grey areas indicate where the angle between the spin plane and magnetic field direction is  $< 15^\circ$ . (Adapted from Puhl-Quinn et al. 2008)

spin plane, in which two pairs of EFW double probes lie, is in the  $X$ - $Y$  plane of DSI coordinates. The shaded areas in the figure correspond to the region where the angle between the spin plane and magnetic field direction is  $< 15^\circ$ . In this region, the third component of the electric field cannot be determined reliably by the EFW measurements through the assumption of  $\mathbf{E} \cdot \mathbf{B} = 0$ . In Fig. 16a (2 October 2001), EDI measurements are available in the shaded region, while EFW data are missing. In contrast, there are many EDI data gaps near CLUSTER perigee, while EFW tends to get data at these times. In this example, the two instruments are complementary. In Fig. 16b (18 April 2002), EDI data are not available, in most part, around the magnetic equator. Nevertheless, EFW worked well during this orbit. This period corresponds to a major storm with sawtooth signatures (e.g., Huang et al. 2005; Ohtani et al. 2007). In Fig. 16c (4 July 2001), both EDI and EFW get data continuously. There are, however, offsets between EDI and EFW data around the magnetic equator. EDI data appear to have smaller errors compared to EFW data. The spurious electric field in the EFW data has a general dependence on the spacecraft potential with the components parallel to the following directions: (i) sunward; (ii) magnetic field; (iii) spacecraft velocity; and (iv) plasma convection. The former two components are related to the photoelectron cloud around the spacecraft. The latter two components are related to wakes created by the relative motion between the spacecraft and the plasma, which was previously reported by Eriksson et al. (2006).

So far an inner magnetospheric electric field model, termed the UNH-IMEF model, has been developed based on a large database merging EDI and EFW data (Matsui et al. 2008). The EDI data are used whenever they are available. If EDI data are missing, EFW data are used by compensating the average offsets between EFW and EDI data for each 5 minutes. The average electric field patterns in two dimensional space sorted by  $L$  value and MLT are generated after mapping in situ CLUSTER data at magnetic latitudes within  $\sim \pm 50^\circ$  of the magnetic equator. The mapping of the electric field is performed so that plasma motion at in situ spacecraft locations ( $> 3R_E$  altitude) is consistent with that at the magnetic equator

on a magnetic field line predicted by Tsyganenko (2002). The equipotential assumption is still the basis for such mapping. The mapping distance between CLUSTER locations and the magnetic equator, however, is smaller than the distance between the ionosphere and the equator so that the reliance on the equipotential assumption is less. The organizing parameter for the inner magnetospheric electric field is the interplanetary electric field (IEF) defined as

$$IEF = vB_z \sin^2(\theta/2), \tag{17}$$

where  $v$  is the solar wind velocity,  $B_z$  is the IMF  $z$  component, and  $\theta$  is the IMF clock angle defined as  $\theta = \tan^{-1}(B_y/B_z)$  with  $B_y$  corresponding to the IMF  $y$  component. The relation between the electric field pattern and the electric potential pattern is given by

$$\mathbf{e} = \mathbf{A}\boldsymbol{\phi}, \tag{18}$$

where  $\mathbf{e}$  is a vector, which consists of electric field vectors from all two-dimensional spatial bins in polar coordinates organized by  $L$  values and MLT,  $\mathbf{A}$  is an operator to calculate the spatial gradient, and  $\boldsymbol{\phi}$  is a vector, which consists of electric potential values from all spatial bins (Matsui et al. 2004). Since the potential is calculated from the electric field, this is regarded as an inverse problem because the electric field is derived from the electric potential in (18). The electric potential is practically estimated by

$$\hat{\boldsymbol{\phi}} = (\mathbf{A}^T \mathbf{A} + \gamma \mathbf{C}^T \mathbf{C})^{-1} \mathbf{A}^T \mathbf{e}, \tag{19}$$

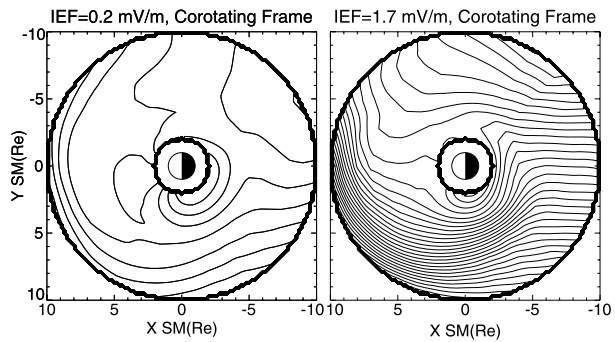
where  $\hat{\boldsymbol{\phi}}$  is the estimated potential,  $\gamma$  is a trade-off parameter,  $\mathbf{C}$  is a regular matrix, which is a Laplacian operator. If the parameter  $\gamma$  decreases, the equation is close to the original equation (18), although the error is not reduced. If the parameter  $\gamma$  increases, the result is smoothed too much by the Laplacian operator. The criterion for choosing the proper  $\gamma$  is discussed by Korth et al. (2002) and is determined by using the following equation

$$\sigma^2 = \frac{\|\mathbf{A}\hat{\boldsymbol{\phi}} - \mathbf{e}\|^2}{N_e - N_\phi}, \tag{20}$$

where  $N_e$  is the number of data points and  $N_\phi$  is the number of model parameters we determined and is given by the trace of the matrix  $(\mathbf{A}^T \mathbf{A} + \gamma \mathbf{C}^T \mathbf{C})^{-1} \mathbf{A}^T \mathbf{A}$  (Tarantola 1987). A proper  $\gamma$  is obtained when  $\sigma^2$  starts to increase.

In the UNH-IMEF model, statistical results are organized by the interplanetary electric field derived from the Advanced Composition Explorer (ACE) spacecraft (see (17)). ACE magnetic field and plasma moment data (McComas et al. 1998; Smith et al. 1998) are used. ACE is located at the L1 point ( $\sim 200 R_E$  upstream from the Earth) so that the solar wind at the ACE location typically arrives at the Earth several tens of minutes later. The organization of CLUSTER data by ACE data makes it possible to use the model for prediction. The model is developed using the method proposed in the previous statistical analysis (Matsui et al. 2004) with the larger database merging the EDI and EFW data. The electric field calculated with the UNH-IMEF model is used as an input parameter for the ring current-atmosphere interaction model (RAM) (Jordanova et al. 2003) in order to validate the UNH-IMEF model. The RAM model simulates time evolution of the spatial distribution of ring current particles. The  $Dst$  index can be reproduced from the ring current distribution by using the Dessler-Parker-Sckopke relation (Dessler and Parker 1959; Sckopke 1966) and can be compared with the measured values. If the simulated and measured values match, the UNH-IMEF electric field model is possibly reliable. There are other ways to validate the model. The

**Fig. 17** Electric potential patterns derived in the corotating frame at IEF = 0.2 and 1.7  $\text{mV m}^{-1}$ . Contour intervals are 1 and 5 kV for *thin* and *thick* lines, respectively



calculated location of the LCE is dependent on the electric field model used. The UNH-IMEF model could be used to predict the location of the LCE, and then comparisons could be made with observations of the plasmapause during extended quiet times when the LCE and plasmapause should coincide.

This version of the UNH-IMEF has been made public (<http://edi.sr.unh.edu/unh-imef/>). Figure 17 shows two examples of potential patterns with IEF = 0.2 and 1.7  $\text{mV m}^{-1}$  in the corotating frame. The electric field strength increases as the IEF increases. The equipotential contours often rotate around the Earth on the dusk-side, indicating ionospheric shielding of the electric field. There are still two points to be checked concerning the performance of the model. The first point is the comparison between the average electric field and the electric field derived from the potential pattern. This is related to the validity of assuming time-stationarity in the above statistical treatment (Faraday's law), which is not always satisfied (Matsui et al. 2004). The second point is the comparison of model results with instantaneous CLUSTER measurements. The model is not yet optimized to include effects of the sub-auroral polarization stream (SAPS). Goldstein et al. (2005) derived a SAPS electric potential model by referring to statistical results on SAPS using DMSP data by Foster and Vo (2002). It would be worthwhile to update the UNH-IMEF model to include SAPS.

### 5.3 Influence of Electric Field Models on the Plasmapause Position Modeling

The convection electric field appears to be a key factor in the formation of the plasmapause and very different results are obtained depending on the characteristics of the electric field model. Pierrard et al. (2008a) have determined how three magnetospheric electric field models influence the radial distance, the shape and the evolution of the plasmapause during the geomagnetic storms of 28 October 2001 and of 17 April 2002. These models are the VSMC model, the E5D model, and the model of Weimer (1996) described in the previous section. Two different mechanisms proposed for the formation of the plasmapause have been studied: (i) the interplay of magnetospheric convection and plasma corotation with the Earth in which the plasmapause should correspond to the LCE or last-closed-streamline (LCS), if the electric field distribution is stationary or time-dependent respectively (Grebowsky 1970); (ii) the interchange mechanism where the plasmapause corresponds to streamlines tangent to a Zero-Parallel-Force surface where the field-aligned plasma distribution becomes connectively unstable during enhancements of the electric field intensity in the nightside local time sector (Lemaire and Pierrard 2008).

Using the same mechanism for plasmapause formation, the plasmapause is obtained to be further away from the Earth with E5D than with the other models. The plasmapause position obtained with the E5D model and the interchange mechanism is closer to the EUV

observations during the geomagnetic storms of 28 October 2001 and 17 April 2002 than the positions obtained with other electric fields models and LCS (interplay between the convection and corotation) simulations. The LCS simulations using the E5D electric field model systematically produce a plasmopause position that is too far away. Results of LCS simulations are improved using the VSMC model, which has been fitted in order to match the LCE with observed plasmopause positions. Although the plasmopause positions of different simulations are found to be quite different, an interesting recent result is that all of the different electric field models account for the formation of plumes during magnetic storms (Pierrard et al. 2008a).

The results of different time dependent simulations were successfully compared with concomitant EUV/IMAGE observations when available (Pierrard and Cabrera 2005, 2006; Pierrard 2006) and also with CIS/IMAGE (Dandouras et al. 2005) and CLUSTER observations (Darrouzet et al. 2006; Schäfer et al. 2007, 2008). Combined with the kinetic model of the plasmasphere developed by Pierrard and Lemaire (2001), dynamic simulations of plasmopause formation give a full description of the plasmasphere in three dimensions (Pierrard and Stegen 2008). The core of this plasmaspheric model is obtained from the kinetic exospheric approach assuming a kappa velocity distribution function for particles. Note that the frequency spectrum of plasma resonances stimulated by the IMAGE/RPI transmissions in the inner magnetosphere, but outside the plasmopause, was consistent with a kappa electron-velocity distribution with a low kappa value (Viñas et al. 2005). The relative abundance of trapped particles is constrained in such way that density profiles correspond to satellite observations. This analytical model is semi-empirical, but incorporates major physical features that determine the density distributions in flux tubes at high altitudes.

Liemohn et al. (2004) have also compared some electric field models and their effects on plasmaspheric morphologies. They used a modified McIlwain electric field model, Weimer model, and another self-consistent electric potential model for the time span of the recovery phase of the 17 April 2002 magnetic storm. These authors found that all these models have certain strengths but also weaknesses in predicting the observed plasmopause position during this storm. They found especially that the electric field intensity of Weimer's model was too strong in the inner magnetosphere, leading to a plasmopause that was too small. Liemohn's modified McIlwain model (which differs from the original E5D model) has too small an electric field intensity around noon, leading to a plasmopause position that does not correspond to the EUV observations on the dayside, although a good fit was obtained in the nightside.

## 6 Summary

Previous empirical models of plasma number and mass densities in the inner magnetosphere have been developed by statistical, time-aliased averaging of a large set of in situ measurements. The advent of the IMAGE RPI has added to previous efforts by providing nearly instantaneous measurements of the true field-aligned plasma electron densities, 2-dimensional profiles of density across 20-minute or so orbital passes and repeated transits of inner magnetospheric space over more than 5-years. New, advanced empirical models of plasma density in the plasmasphere and polar cap have resulted. The new plasmaspheric density model not only refines and confirms the radial distance and latitude dependence established using in situ measurements, but has for the first time revealed the density distribution along depleted magnetic field lines. The new polar cap density models are significantly more comprehensive, by refining and going beyond the radial distance density dependence represented in previous empirical models to include latitude and local time dependence through solar zenith angles at ionospheric altitudes. Furthermore, the newly developed polar cap models include

geomagnetic activity dependence, which is found to be stronger with increasing altitude. Further exploration of the RPI sounding data in combination with in situ data provided by the passive measurements of RPI and other satellite instruments can be expected to yield even more comprehensive empirical density models of the inner magnetosphere, organized by location, geomagnetic activity, and solar wind parameters.

The CLUSTER multiple-point and multiple-instrument measurements of inner magnetospheric electric fields have made it possible to develop new electric field models. The assumption of equipotential magnetic field lines has been adopted to map the electric field at magnetic latitudes within  $\pm\sim 50^\circ$  of the magnetic equator. Compared to the mapping of the electric field from the ionospheric altitude to the equator, the equipotential assumption has less effects on the equatorial electric fields in the UNH-IMEF model. A large database of CLUSTER EDI and EFW measurements have been merged to create a new empirical model of the inner magnetospheric electric field. Further development of the new electric field model is underway using additional merging of electric fields derived from CLUSTER CIS and FGM measurements.

The electric field distribution is critical in modeling the plasmasphere dynamics. An interesting result is that all of the electric field models that have been obtained account for the formation of plumes during geomagnetic storms. None of the electrostatic field models, however, are capable yet of fully reproducing the magnetospheric electric field distribution. There remains a long way to go before the detailed structures observed in the EUV observations during periods of enhanced geomagnetic activity can be accounted for by an electric field model. These studies point out the need to develop higher time resolution empirical models for the magnetospheric electrostatic field distribution like those developed for the geomagnetic field. The empirical electric field models being developed using the CLUSTER multiple-point and multiple-instrument dataset, such as UNH-IMEF, will hopefully meet this need.

**Acknowledgements** The work at UML was supported by NASA grant NNX07AG38G, NASA grant via subcontract 83822 from SwRI, NSF grant 0518227, and AFRL contract FA8718-06-C-0072 to the University of Massachusetts Lowell. The work at Dartmouth College was supported by NSF grants ATM-0632740 and ATM-0120950 (Center for Integrated Space Weather Modeling, CISM, funded by the Science and Technology Centers Program). This paper is an outcome of the workshop "The Earth's plasmasphere: A CLUSTER, IMAGE, and modeling perspective", organized by the Belgian Institute for Space Aeronomy in Brussels in September 2007. The use of Figs. 2, 3, 5 and 6 is with the permission of Elsevier.

## References

- A. Balogh, C.M. Carr, M.H. Acuña, M.W. Dunlop, T.J. Beek, P. Brown, K.H. Fornaçon, E. Georgescu, K.H. Glassmeier, J. Harris, G. Musmann, T. Oddy, K. Schwingschuh, The Cluster Magnetic Field Investigation: overview of in-flight performance and initial results. *Ann. Geophys.* **19**(10–12), 1207–1217 (2001)
- R.F. Benson, P.A. Webb, J.L. Green, L. Garcia, B.W. Reinisch, Magnetospheric electron densities inferred from upper-hybrid band emissions. *Geophys. Res. Lett.* **31**, L20803 (2004)
- D. Berube, M.B. Moldwin, S.F. Fung, J.L. Green, A plasmaspheric mass density model and constraints on its heavy ion concentration. *J. Geophys. Res.* **110**, A04212 (2005)
- D. Bilitza, International Reference Ionosphere 2000. *Radio Sci.* **36**(2), 261–275 (2001)
- J.H. Binsack, Plasmopause observations with the M.I.T. experiment on IMP 2. *J. Geophys. Res.* **72**(21), 5231–5237 (1967)
- A. Boonsiriseth, R. Thorne, G. Lu, V.K. Jordanova, M.F. Thomsen, D.M. Ober, A.J. Ridley, A semiempirical equatorial mapping of AMIE convection electric potentials (MACEP) for the January 10, 1997, magnetic storm. *J. Geophys. Res.* **106**(A7), 12903–12917 (2001)
- J.L. Burch, IMAGE mission overview. *Space Sci. Rev.* **91**(1–2), 1–14 (2000)
- J.L. Burch, The first two years of image. *Space Sci. Rev.* **109**(1–4), 1–24 (2003)

- J.F. Carbary, A  $K_p$ -based model of auroral boundaries. *Space Weather* **3**(10), 10001 (2005)
- D.L. Carpenter, Whistler evidence of a “knee” in the magnetospheric ionization density profile. *J. Geophys. Res.* **68**(6), 1675–1682 (1963)
- D.L. Carpenter, Whistler studies of the plasmapause in the magnetosphere, 1. Temporal variations in the position of the knee and some evidence on plasma motions near the knee. *J. Geophys. Res.* **71**(3), 693–709 (1966)
- D.L. Carpenter, Remote sensing the Earth’s plasmasphere. *Radio Sci. Bull.* **308**, 13–29 (2004)
- D.L. Carpenter, R.R. Anderson, An ISEE/whistler model of equatorial electron density in the magnetosphere. *J. Geophys. Res.* **97**(A2), 1097–1108 (1992)
- D.L. Carpenter, J. Lemaire, Erosion and recovery of the plasmasphere in the plasmapause region. *Space Sci. Rev.* **80**(1–2), 153–179 (1997)
- C.R. Chappell, K.K. Harris, G.W. Sharp, The dayside of the plasmasphere. *J. Geophys. Res.* **76**(31), 7632–7647 (1971)
- M.A. Clilverd, A.J. Smith, N.R. Thomson, The annual variation in quiet time plasmaspheric electron density, determined from whistler mode group delays. *Planet. Space Sci.* **39**(7), 1059–1067 (1991)
- P.D. Craven, D.L. Gallagher, R.H. Comfort, Relative concentration of  $\text{He}^+$  in the inner magnetosphere as observed by the DE 1 retarding ions mass spectrometer. *J. Geophys. Res.* **102**(A2), 2279–2289 (1997)
- I. Dandouras, V. Pierrard, J. Goldstein, C. Vallat, G.K. Parks, H. Rème, C. Goullart, F. Sevestre, M. McCarthy, L.M. Kistler, B. Klecker, A. Korth, M.B. Bavassano-Cattaneo, P. Escoubet, A. Masson, Multipoint observations of ionic structures in the plasmasphere by CLUSTER-CIS and comparisons with IMAGE-EUV observations and with model simulations, in *Inner Magnetosphere Interactions: New Perspectives from Imaging*, ed. by J.L. Burch, M. Schulz, H. Spence. Geophysical Monograph Series, vol. 159 (American Geophysical Union, Washington, 2005), pp. 23–53
- F. Darrouzet, J. De Keyser, P.M.E. Décréau, D.L. Gallagher, V. Pierrard, J.F. Lemaire, B.R. Sandel, I. Dandouras, H. Matsui, M. Dunlop, J. Cabrera, A. Masson, P. Canu, J.G. Trotignon, J.L. Rauch, M. André, Analysis of plasmaspheric plumes: CLUSTER and IMAGE observations. *Ann. Geophys.* **24**(6), 1737–1758 (2006)
- J. De Keyser, D.L. Carpenter, F. Darrouzet, D.L. Gallagher, J. Tu, CLUSTER and IMAGE: New ways to study the Earth’s plasmasphere. *Space Sci. Rev.* (2008), this issue
- P.M.E. Décréau, C. Beghin, M. Parrot, Global characteristics of the cold plasma in the equatorial plasmapause region as deduced from the GEOS 1 mutual impedance probe. *J. Geophys. Res.* **87**(A2), 695–712 (1982)
- C.F. del Pozo, M. Blanc, Analytical self-consistent model of the large-scale convection electric field. *J. Geophys. Res.* **99**(A3), 4053–4068 (1994)
- R.E. Denton, Magneto-seismology using spacecraft observations, in *Magnetospheric ULF Waves: Synthesis and New Directions*, ed. by K. Takahashi, P.J. Chi, R.E. Denton, R.L. Lysak. Geophysical Monograph Series, vol. 169 (American Geophysical Union, Washington, 2006), pp. 307–317
- R.E. Denton, J. Goldstein, J.D. Menietti, Field line dependence of magnetospheric electron density. *Geophys. Res. Lett.* **29**(24), 2205 (2002a)
- R.E. Denton, J. Goldstein, J.D. Menietti, S.L. Young, Magnetospheric electron density model inferred from Polar plasma wave data. *J. Geophys. Res.* **107**(A11), 1386 (2002b)
- R.E. Denton, J.D. Menietti, J. Goldstein, S.L. Young, R.R. Anderson, Electron density in the magnetosphere. *J. Geophys. Res.* **109**, A09215 (2004)
- R.E. Denton, J. Goldstein, D.H. Lee, R.A. King, Z.C. Dent, D.L. Gallagher, D. Berube, K. Takahashi, M. Nose, D. Milling, F. Honary, Realistic magnetospheric density model for 29 August 2000. *J. Atmos. Sol. Terr. Phys.* **68**(6), 615–628 (2006a)
- R.E. Denton, K. Takahashi, I.A. Galkin, P.A. Nsumei, X. Huang, B.W. Reinisch, R.R. Anderson, M.K. Sleeper, W.J. Hughes, Distribution of density along magnetospheric field lines. *J. Geophys. Res.* **111**, A04213 (2006b)
- R.E. Denton, P. Décréau, M.J. Engebretson, F. Darrouzet, J.L. Posch, C. Moukikis, L.M. Kistler, C.A. Cattell, K. Takahashi, S. Schäfer, J. Goldstein, Field line distribution of density at  $L = 4.8$  inferred from observations by CLUSTER. *Ann. Geophys.* (2009, in press)
- A.J. Dessler, E.N. Parker, Hydromagnetic theory of geomagnetic storms. *J. Geophys. Res.* **64**(12), 2239–2252 (1959)
- Y. Ebihara, M. Ejiri, Numerical simulation of the ring current: Review. *Space Sci. Rev.* **105**(1–2), 377–452 (2002)
- A.I. Eriksson, M. André, B. Klecker, H. Laakso, P.-A. Lindqvist, F. Mozer, G. Paschmann, A. Pedersen, J. Quinn, R. Torbert, K. Torkar, H. Vaith, Electric field measurements on Cluster: comparing the double-probe and electron drift techniques. *Ann. Geophys.* **24**(1), 275–289 (2006)
- C.P. Escoubet, C.T. Russell, R. Schmidt (eds.), *The Cluster and Phoenix Missions* (Kluwer Academic, Dordrecht, 1997), p. 658

- Y.I. Feldstein, A.E. Levitin, D.S. Faermark, R.G. Afonina, B.A. Belov, V.Y. Gaidukov, Electric fields and potential patterns in the high-latitude ionosphere for different situations in interplanetary space. *Planet. Space Sci.* **32**(7), 907–923 (1984)
- J.C. Foster, H.B. Vo, Average characteristics and activity dependence of the subauroral polarization stream. *J. Geophys. Res.* **107**(A12), 1475 (2002)
- S.F. Fung, J.L. Green, Modeling of field-aligned guided echoes in the plasmasphere. *J. Geophys. Res.* **110**, A01210 (2005)
- S.F. Fung, L.N. Garcia, J.L. Green, D.L. Gallagher, D.L. Carpenter, B.W. Reinisch, I.A. Galkin, G. Khmyrov, B.R. Sandel, Plasmaspheric electron density distributions sampled by Radio Plasma Imager on the IMAGE satellite. *Eos Trans. AGU* **82**(47), SM11A–0771 (2001)
- S.F. Fung, R.F. Benson, D.L. Carpenter, J.L. Green, V. Jayanti, I.A. Galkin, B.W. Reinisch, Guided echoes in the magnetosphere: Observations by Radio Plasma Imager on IMAGE. *Geophys. Res. Lett.* **30**(11), 1589 (2003)
- I. Galkin, B. Reinisch, G. Grinstein, G. Khmyrov, A. Kozlov, X. Huang, S. Fung, Automated exploration of the radio plasma imager data. *J. Geophys. Res.* **109**, A12210 (2004)
- D.L. Gallagher, P.D. Craven, R.H. Comfort, A simple model of magnetospheric trough total density. *J. Geophys. Res.* **103**(A5), 9293–9297 (1998)
- D.L. Gallagher, P.D. Craven, R.H. Comfort, Global core plasma model. *J. Geophys. Res.* **105**(A8), 18819–18833 (2000)
- D.L. Gallagher, M.L. Adrian, M.W. Liemohn, Origin and evolution of deep plasmaspheric notches. *J. Geophys. Res.* **110**, A09201 (2005)
- J. Goldstein, M. Spasojević, P.H. Reiff, B.R. Sandel, W.T. Forrester, D.L. Gallagher, B.W. Reinisch, Identifying the plasmopause in IMAGE EUV data using IMAGE RPI in situ steep density gradients. *J. Geophys. Res.* **108**(A4), 1147 (2003)
- J. Goldstein, J.L. Burch, B.R. Sandel, Magnetospheric model of subauroral polarization stream. *J. Geophys. Res.* **110**, A09222 (2005)
- J.M. Grebowsky, Model study of plasmopause motion. *J. Geophys. Res.* **75**(22), 4329–4333 (1970)
- J.L. Green, B.W. Reinisch, An overview of results from RPI on Image. *Space Sci. Rev.* **109**(1–4), 183–210 (2003)
- K.I. Gringauz, The structure of the ionized gas envelope of the Earth from direct measurements in the USSR of local charged particle concentrations. *Planet. Space Sci.* **11**(3), 281–296 (1963)
- G. Gustafsson, M. André, T. Carozzi, A.I. Eriksson, C.G. Fälthammar, R. Grard, G. Holmgren, J.A. Holtet, N. Ivchenko, T. Karlsson, Y. Khotyaintsev, S. Klimov, H. Laakso, P.-A. Lindqvist, B. Lybekk, G. Marklund, F. Mozer, K. Mursula, A. Pedersen, B. Popielawska, S. Savin, K. Stasiewicz, P. Tanskanen, A. Vaivads, J.-E. Wahlund, First results of electric field and density observations by Cluster EFW based on initial months of observations. *Ann. Geophys.* **19**(10–12), 1219–1240 (2001)
- R.A. Heelis, J.K. Lowell, R.W. Spiro, A model of the high-latitude ionospheric convection pattern. *J. Geophys. Res.* **87**(A8), 6339–6345 (1982)
- J.P. Heppner, Empirical models of high-latitude electric fields. *J. Geophys. Res.* **82**(7), 1115–1125 (1977)
- J.P. Heppner, N.C. Maynard, Empirical high-latitude electric field models. *J. Geophys. Res.* **92**(A5), 4467–4489 (1987)
- J.M. Holt, R.H. Wand, J.V. Evans, W.L. Oliver, Empirical models for the plasma convection at high latitudes from millstone hill observations. *J. Geophys. Res.* **92**(A1), 203–212 (1987)
- J.L. Horwitz, S. Menteer, J. Turnley, J.L. Burch, J.D. Winningham, C.R. Chappell, J.D. Craven, L.A. Frank, D.W. Slater, Plasma boundaries in the inner magnetosphere. *J. Geophys. Res.* **91**(A8), 8861–8882 (1986)
- J.L. Horwitz, R.H. Comfort, C.R. Chappell, A statistical characterization of plasmasphere density structure and boundary locations. *J. Geophys. Res.* **95**(A6), 7937–7947 (1990)
- C.S. Huang, G.D. Reeves, G. Le, K. Yumoto, Are sawtooth oscillations of energetic plasma particle fluxes caused by periodic substorms or driven by solar wind pressure enhancements? *J. Geophys. Res.* **110**, A07207 (2005)
- X. Huang, B.W. Reinisch, Automatic calculation of electron density profiles from digital ionograms 2. True height inversion of topside ionograms with the profile-fitting method. *Radio Sci.* **17**(4), 837–844 (1982)
- X. Huang, B.W. Reinisch, P. Song, J.L. Green, D.L. Gallagher, Developing an empirical density model of the plasmasphere using IMAGE/RPI observations. *Adv. Space Res.* **33**(6), 829–832 (2004)
- M.T. Johnson, J.R. Wygant, C. Cattell, F.S. Mozer, M. Temerin, J. Scudder, Observations of the seasonal dependence of the thermal plasma density in the southern hemisphere auroral zone and polar cap at 1  $R_E$ . *J. Geophys. Res.* **106**(A9), 19023–19033 (2001)
- M.T. Johnson, J.R. Wygant, C.A. Cattell, F.S. Mozer, Seasonal variations along auroral field lines: Measurements from the Polar spacecraft. *Geophys. Res. Lett.* **30**(6), 1344 (2003)

- V.K. Jordanova, L.M. Kistler, C.J. Farrugia, R.B. Torbert, Effects of inner magnetospheric convection on ring current dynamics: March 10–12, 1998. *J. Geophys. Res.* **106**(A12), 29705–29720 (2001)
- V.K. Jordanova, A. Boonsiriseth, R.M. Thorne, Y. Dotan, Ring current asymmetry from global simulations using a high-resolution electric field model. *J. Geophys. Res.* **108**(A12), 1443 (2003)
- G.V. Khazanov, M.W. Liemohn, T.S. Newman, M.C. Fok, A.J. Ridley, Magnetospheric convection electric field dynamics and stormtime particle energization: case study of the magnetic storm of 4 May 1998. *Ann. Geophys.* **22**(2), 497–510 (2004)
- M.G. Kivelson, C.T. Russell (eds.), *Introduction to Space Physics* (Cambridge University Press, New York, 1995), p. 594
- H. Korth, M.F. Thomsen, K.H. Glassmeier, W.S. Phillips, Particle tomography of the inner magnetosphere. *J. Geophys. Res.* **107**(A9), 1229 (2002)
- B.A. Larsen, D.M. Klumpar, C. Gurgiolo, Correlation between plasmopause position and solar wind parameters. *J. Atmos. Sol. Terr. Phys.* **69**(3), 334–340 (2007)
- M.J. LeDocq, D.A. Gurnett, R.R. Anderson, Electron number density fluctuations near the plasmopause observed by the CRRES spacecraft. *J. Geophys. Res.* **99**(A12), 23661–23671 (1994)
- J.F. Lemaire, K.I. Gringauz, *The Earth's Plasmasphere* (Cambridge University Press, New York, 1998), p. 372
- J.F. Lemaire, V. Pierrard, Comparison between two theoretical mechanisms for the formation of the plasmopause and relevant observations. *Geomagn. Aeron.* **48**(5), 553–570 (2008)
- M.W. Liemohn, A.J. Ridley, D.L. Gallagher, D.M. Ober, J.U. Kozyra, Dependence of plasmaspheric morphology on the electric field description during the recovery phase of the 17 April 2002 magnetic storm. *J. Geophys. Res.* **109**, A03209 (2004)
- T.M. Loto'aniu, C.L. Waters, B.J. Fraser, J.C. Samson, Plasma mass density in the plasmatrough: Comparison using ULF waves and CRRES. *Geophys. Res. Lett.* **26**(21), 3277–3280 (1999)
- L.R. Lyons, D.J. Williams (eds.), *Quantitative Aspects of Magnetospheric Physics* (Reidel, Dordrecht, 1984), p. 231
- H. Matsui, V.K. Jordanova, J.M. Quinn, R.B. Torbert, G. Paschmann, Derivation of electric potential patterns in the inner magnetosphere from Cluster EDI data: Initial results. *J. Geophys. Res.* **109**, A10202 (2004)
- H. Matsui, P.A. Puhl-Quinn, V.K. Jordanova, Y. Khotyaintsev, P.-A. Lindqvist, R.B. Torbert, Derivation of inner magnetospheric electric field (UNH-IMEF) model using Cluster data set. *Ann. Geophys.* **26**(9), 2887–2898 (2008)
- N.C. Maynard, A.J. Chen, Isolated cold plasma regions: observations and their relation to possible production mechanisms. *J. Geophys. Res.* **80**(7), 1009–1013 (1975)
- D.J. McComas, S.J. Bame, P. Barker, W.C. Feldman, J.L. Phillips, P. Riley, J.W. Griffee, Solar Wind Electron Proton Alpha Monitor (SWEPAM) for the Advanced Composition Explorer. *Space Sci. Rev.* **86**(1–4), 563–612 (1998)
- C.E. McIlwain, A Kp dependent equatorial electric field model. *Adv. Space Res.* **6**(3), 187–197 (1986)
- F.W. Menk, D. Orr, M.A. Clilverd, A.J. Smith, C.L. Waters, D.K. Milling, B.J. Fraser, Monitoring spatial and temporal variations in the dayside plasmasphere using geomagnetic field line resonances. *J. Geophys. Res.* **104**(A9), 19955–19969 (1999)
- M.B. Moldwin, M.F. Thomsen, S.J. Bame, D.J. McComas, K.R. Moore, An examination of the structure and dynamics of the outer plasmasphere using multiple geosynchronous satellites. *J. Geophys. Res.* **99**(A6), 11475–11481 (1994)
- M.B. Moldwin, L. Downward, H.K. Rassoul, R. Amin, R.R. Anderson, A new model of the location of the plasmopause: CRRES results. *J. Geophys. Res.* **107**(A11), 1339 (2002)
- T.E. Moore, W.K. Peterson, C.T. Russell, M.O. Chandler, M.R. Collier, H.L. Collin, P.D. Craven, R. Fitzenreiter, B.L. Giles, C.J. Pollock, Ionospheric mass ejection in response to a CME. *Geophys. Res. Lett.* **26**(15), 2339–2342 (1999)
- F.S. Mozer, C.A. Cattell, M. Temerin, R.B. Torbert, S. Von Glinski, M. Woldorff, J. Wygant, The DC and AC electric field, plasma density, plasma temperature, and field-aligned current experiments on the S3-3 satellite. *J. Geophys. Res.* **84**(A10), 5875–5884 (1979)
- A. Nishida, Formation of plasmopause, or magnetospheric plasma knee, by the combined action of magnetospheric convection and plasma escape from the tail. *J. Geophys. Res.* **71**(23), 5669–5679 (1966)
- P.A. Nsumei, X. Huang, B.W. Reinisch, P. Song, V.M. Vasyliunas, J.L. Green, S.F. Fung, R.F. Benson, D.L. Gallagher, Electron density distribution over the northern polar region deduced from IMAGE/radio plasma imager sounding. *J. Geophys. Res.* **108**(A2), 1078 (2003)
- P.A. Nsumei, B.W. Reinisch, P. Song, J. Tu, X. Huang, Polar cap electron density distribution from IMAGE radio plasma imager measurements: Empirical model with the effects of solar illumination and geomagnetic activity. *J. Geophys. Res.* **113**, A01217 (2008)
- T.P. O'Brien, M.B. Moldwin, Empirical plasmopause models from magnetic indices. *Geophys. Res. Lett.* **30**(4), 1152 (2003)

- S. Ohtani, H. Korth, P.C. Brandt, L.G. Blomberg, H.J. Singer, M.G. Henderson, E.A. Lucek, H.U. Frey, Q. Zong, J.M. Weygand, Y. Zheng, A.T.Y. Lui, Cluster observations in the inner magnetosphere during the 18 April 2002 sawtooth event: Dipolarization and injection at  $r = 4.6 R_E$ . *J. Geophys. Res.* **112**, A08213 (2007)
- V.A. Osherovich, R.F. Benson, J. Fainberg, J.L. Green, L. Garcia, S. Boardsen, N. Tsyganenko, B.W. Reinisch, Enhanced high-altitude polar cap plasma and magnetic field values in response to the interplanetary magnetic cloud that caused the great storm of 31 March 2001: A case study for a new magnetospheric index. *J. Geophys. Res.* **112**, A06247 (2007)
- V.O. Papitashvili, B.A. Belov, D.S. Faermark, Y.I. Feldstein, S.A. Golyshev, L.I. Gromova, A.E. Levitin, Electric potential patterns in the northern and southern polar regions parameterized by the interplanetary magnetic field. *J. Geophys. Res.* **99**(A7), 13251–13262 (1994)
- C.G. Park, D.L. Carpenter, D.B. Wiggin, Electron density in the plasmasphere: Whistler data on solar cycle, annual, and diurnal variations. *J. Geophys. Res.* **83**(A7), 3137–3144 (1978)
- G. Paschmann, J.M. Quinn, R.B. Torbert, H. Vaith, C.E. McIlwain, G. Haerndel, O.H. Bauer, T. Bauer, W. Baumjohann, W. Fillius, M. Förster, S. Frey, E. Georgescu, S.S. Kerr, C.A. Kletzing, H. Matsui, P. Puhl-Quinn, E.C. Whipple, The Electron Drift Instrument on Cluster: overview of first results. *Ann. Geophys.* **19**(10–12), 1273–1288 (2001)
- A.M. Persoon, D.A. Gurnett, S.D. Shawhan, Polar cap electron densities from DE 1 plasma wave observations. *J. Geophys. Res.* **88**(A12), 10123–10136 (1983)
- V. Pierrard, The dynamics of the plasmasphere, in *Space Science: New Research*, ed. by N.S. Maravell (Nova Science, New York, 2006), pp. 83–96
- V. Pierrard, J. Cabrera, Comparisons between EUV/IMAGE observations and numerical simulations of the plasmopause formation. *Ann. Geophys.* **23**(7), 2635–2646 (2005)
- V. Pierrard, J. Cabrera, Dynamical simulations of plasmopause deformations. *Space Sci. Rev.* **122**(1–4), 119–126 (2006)
- V. Pierrard, J. Lemaire, Exospheric model of the plasmasphere. *J. Atmos. Sol. Terr. Phys.* **63**(11), 1261–1265 (2001)
- V. Pierrard, K. Stegen, A three-dimensional dynamic kinetic model of the plasmasphere. *J. Geophys. Res.* **113**, A10209 (2008)
- V. Pierrard, G.V. Khazanov, J. Cabrera, J. Lemaire, Influence of the convection electric field models on predicted plasmopause positions during magnetic storms. *J. Geophys. Res.* **113** A08212 (2008a)
- V. Pierrard, J. Goldstein, N. André, V.K. Jordanova, G.A. Kotova, J.F. Lemaire, M.W. Liemohn, H. Matsui, Recent progress in physics-based models of the plasmasphere. *Space Sci. Rev.* (2008b), this issue
- J.H. Pope, An estimate of electron densities in the exosphere by means of Nose Whistlers. *J. Geophys. Res.* **66**(1), 67–75 (1961)
- I.A. Price, C.L. Waters, F.W. Menk, G.J. Bailey, B.J. Fraser, A technique to investigate plasma mass density in the topside ionosphere using ULF waves. *J. Geophys. Res.* **104**(A6), 12723–12732 (1999)
- P.A. Puhl-Quinn, H. Matsui, V.K. Jordanova, Y. Khotyaintsev, P.A. Lindqvist, An effort to derive an empirically based, inner-magnetospheric electric field model: Merging Cluster EDI and EFW data. *J. Atmos. Sol. Terr. Phys.* **70**(2–4), 564–573 (2008)
- B.W. Reinisch, D.M. Haines, K. Bibl, G. Cheney, I.A. Galkin, X. Huang, S.H. Myers, G.S. Sales, R.F. Benson, S.F. Fung, J.L. Green, S. Boardsen, W.W.L. Taylor, J.L. Bougeret, R. Manning, N. Meyer-Vernet, M. Moncuquet, D.L. Carpenter, D.L. Gallagher, P. Reiff, The Radio Plasma Imager investigation on the IMAGE spacecraft. *Space Sci. Rev.* **91**(1–2), 319–359 (2000)
- B.W. Reinisch, X. Huang, P. Song, G.S. Sales, S.F. Fung, J.L. Green, D.L. Gallagher, V.M. Vasyliunas, Plasma density distribution along the magnetospheric field: RPI observations from IMAGE. *Geophys. Res. Lett.* **28**(24), 4521–4524 (2001a)
- B.W. Reinisch, D.M. Haines, R.F. Benson, J.L. Green, G.S. Sales, W.W.L. Taylor, Radio sounding in space: magnetosphere and topside ionosphere. *J. Atmos. Sol. Terr. Phys.* **63**(2–3), 87–98 (2001b)
- B.W. Reinisch, X. Huang, P. Song, J.L. Green, S.F. Fung, V.M. Vasyliunas, D.L. Gallagher, B.R. Sandel, Plasmaspheric mass loss and refilling as a result of a magnetic storm. *J. Geophys. Res.* **109**, A01202 (2004)
- H. Rème, C. Aoustin, J.M. Bosqued, I. Dandouras, B. Lavraud, J.A. Sauvaud, A. Barthe, J. Bouyssou, Th. Camus, O. Coeur-Joly, A. Cros, J. Cuvalo, F. Ducay, Y. Garbarowitz, J.L. Médale, E. Penou, H. Perrier, D. Romefort, J. Rouzaud, C. Vallat, D. Alcaydé, C. Jacquy, C. Mazelle, C. d’Uston, E. Möbius, L.M. Kistler, K. Crocker, M. Granoff, C. Mouikis, M. Popecki, M. Vosbury, B. Klecker, D. Hovestadt, H. Kucharek, E. Kuenneth, G. Paschmann, M. Scholer, N. Sckopke, E. Seidenschwang, C.W. Carlson, D.W. Curtis, C. Ingraham, R.P. Lin, J.P. McFadden, G.K. Parks, T. Phan, V. Formisano, E. Amata, M.B. Bavassano-Cattaneo, P. Baldetti, R. Bruno, G. Chionchio, A. Di Lellis, M.F. Marcucci, G. Pallochia, A. Korth, P.W. Daly, B. Graeve, H. Rosenbauer, V. Vasyliunas, M. McCarthy, M. Wilber, L. Eliasson, R. Lundin, S. Olsen, E.G. Shelley, S. Fuselier, A.G. Ghielmetti, W. Lennartsson, C.P. Escoubet,

- H. Balsiger, R. Friedel, J.-B. Cao, R.A. Kovrazhkin, I. Papamastorakis, R. Pellat, J. Scudder, B. Sonnerup, First multi-spacecraft ion measurements in and near the Earth's magnetosphere with the identical Cluster Ion Spectrometry (CIS) experiment. *Ann. Geophys.* **19**(10–12), 1303–1354 (2001)
- A.D. Richmond, Y. Kamide, Mapping electrodynamic features of the high-latitude ionosphere from localized observations: Technique. *J. Geophys. Res.* **93**(A6), 5741–5759 (1988)
- J.M. Ruohoniemi, R.A. Greenwald, Dependencies of high-latitude plasma convection: Consideration of interplanetary magnetic field, seasonal, and universal time factors in statistical patterns. *J. Geophys. Res.* **110**, A09204 (2005)
- B.R. Sandel, R.A. King, W.T. Forrester, D.L. Gallagher, A.L. Broadfoot, C.C. Curtis, Initial results from the IMAGE Extreme Ultraviolet Imager. *Geophys. Res. Lett.* **28**(8), 1439–1442 (2001)
- S. Schäfer, K.H. Glassmeier, P.T.I. Eriksson, V. Pierrard, K.H. Fornaçon, L.G. Blomberg, Spatial and temporal characteristics of poloidal waves in the terrestrial plasmasphere: a CLUSTER case study. *Ann. Geophys.* **25**(4), 1011–1024 (2007)
- S. Schäfer, K.H. Glassmeier, P.T.I. Eriksson, P.N. Mager, V. Pierrard, K.H. Fornaçon, L.G. Blomberg, Spatio-temporal structure of a poloidal Alfvén wave detected by Cluster adjacent to the dayside plasmopause. *Ann. Geophys.* **26**(7), 1805–1817 (2008)
- N. Sckopke, A general relation between the energy of trapped particles and the disturbance field near the earth. *J. Geophys. Res.* **71**(13), 3125–3130 (1966)
- B.W. Sheeley, M.B. Moldwin, H.K. Rassoul, R.R. Anderson, An empirical plasmasphere and trough density model: CRRES observations. *J. Geophys. Res.* **106**(A11), 25631–25641 (2001)
- N. Singh, J.L. Horwitz, Plasmaspheric refilling: Recent observations and modelling. *J. Geophys. Res.* **97**(A2), 1049–1079 (1992)
- G. Siscoe, D. Baker, R. Weigel, J. Hughes, H. Spence, Roles of empirical modeling within CISM. *J. Atmos. Sol. Terr. Phys.* **66**(15–16), 1481–1489 (2004)
- C.W. Smith, J. L'Heureux, N.F. Ness, M.H. Acuña, L.F. Burlaga, J. Scheifele, The ACE magnetic fields experiment. *Space Sci. Rev.* **86**(1–4), 613–632 (1998)
- R.L. Smith, Properties of the outer ionosphere deduced from nose whistlers. *J. Geophys. Res.* **66**(11), 3709–3716 (1961)
- J.J. Sojka, C.E. Rasmussen, R.W. Schunk, An interplanetary magnetic field dependent model of the ionospheric convection electric field. *J. Geophys. Res.* **91**(A10), 11281–11290 (1986)
- P. Song, B.W. Reinisch, X. Huang, Magnetospheric active wave measurements. *COSPAR Colloq. Ser.* **16**, 235–246 (2004)
- D.P. Stern, The motion of a proton in the equatorial magnetosphere. *J. Geophys. Res.* **80**(4), 595–599 (1975)
- D.P. Stern, Large-scale electric fields in the Earth's magnetosphere. *Rev. Geophys. Space Phys.* **15**(2), 156–194 (1977)
- L.R.O. Storey, An investigation of whistling atmospherics. *Philos. Trans. R. Soc. (Lond.) A* **246**, 113–141 (1953)
- K. Takahashi, R.E. Denton, R.R. Anderson, W.J. Hughes, Frequencies of standing Alfvén wave harmonics and their implication for plasma mass distribution along geomagnetic field lines: Statistical analysis of CRRES data. *J. Geophys. Res.* **109**, A08202 (2004)
- A. Tarantola, *Inverse Problem Theory* (Elsevier, Amsterdam, 1987), p. 613
- N.A. Tsyganenko, A model of the near magnetosphere with a dawn-dusk asymmetry 1. Mathematical structure. *J. Geophys. Res.* **107**(A8), 1179 (2002)
- N.A. Tsyganenko, D.P. Stern, Modeling the global magnetic field of the large-scale Birkeland current systems. *J. Geophys. Res.* **101**(A12), 27187–27198 (1996)
- J. Tu, J.L. Horwitz, T.E. Moore, Simulating the cleft ion fountain at polar perigee altitudes. *J. Atmos. Sol. Terr. Phys.* **67**(5), 465–477 (2005a)
- J. Tu, P. Song, B.W. Reinisch, X. Huang, J.L. Green, H.U. Frey, P.H. Reiff, Electron density images of the middle- and high-latitude magnetosphere in response to the solar wind. *J. Geophys. Res.* **110**, A12210 (2005b)
- J. Tu, P. Song, B.W. Reinisch, J.L. Green, X. Huang, Empirical specification of field-aligned plasma density profiles for plasmasphere refilling. *J. Geophys. Res.* **111**, A06216 (2006)
- J.N. Tu, M. Dhar, P. Song, B.W. Reinisch, J.L. Green, R.F. Benson, A.J. Coster, Extreme polar cap density enhancements along magnetic field lines during an intense geomagnetic storm. *J. Geophys. Res.* **112**, A05201 (2007)
- A.F. Viñas, R.L. Mace, R.F. Benson, Dispersion characteristics for plasma resonances of Maxwellian and Kappa distribution plasmas and their comparisons to the IMAGE/RPI observations. *J. Geophys. Res.* **110**, A06202 (2005)
- H. Volland, A semiempirical model of large-scale magnetospheric electric fields. *J. Geophys. Res.* **78**(1), 171–180 (1973)

- H. Volland, A model of the magnetospheric electric convection field. *J. Geophys. Res.* **83**(A6), 2695–2699 (1978)
- C.L. Waters, F.W. Menk, M.F. Thomsen, C. Foster, F.R. Fenrich, Remote sensing of the magnetosphere using ground-based observations of ULF waves, in *Magnetospheric ULF Waves: Synthesis and New Directions*, ed. by K. Takahashi, P.J. Chi, R.E. Denton, R.L. Lysak. Geophysical Monograph Series, vol. 169 (American Geophysical Union, Washington, 2006), pp. 319–340
- P.A. Webb, R.F. Benson, R.E. Denton, J. Goldstein, L.N. Garcia, B.W. Reinisch, An inner-magnetospheric electron density database determined from IMAGE/RPI passive dynamic spectra. *EOS Trans. AGU* **88**(52), SM12A–04 (2007)
- D.R. Weimer, A flexible, IMF dependent model of high-latitude electric potentials having “space weather” applications. *Geophys. Res. Lett.* **23**(18), 2549–2552 (1996)
- D.R. Weimer, Improved ionospheric electrodynamic models and application to calculating Joule heating rates. *J. Geophys. Res.* **110**, A05306 (2005)